Characterization of First Phosphate's Lac à l'Orignal Phosphate Deposit, Lac-Saint-Jean Anorthosite (LSJA) Complex, Quebec, Canada: Implications for Supplying Lithium Ferro (Iron) Phosphate (LFP) Batteries

Dr. Sandeep Banerjee

Postdoctoral Researcher
Queen's University, Ontario, Canada
Respectfully Submitted March 13, 2023

EXECUTIVE SUMMARY

The purpose of this report is to describe and interpret the mineralogy, petrology, and geochemistry of First Phosphate's Lac à l'Orignal igneous phosphate deposit. Lac à l'Orignal is part of the Lac-Saint-Jean Anorthosite (LSJA) Complex, Québec, which is the largest anorthosite complex in the world. The primary aim of this partnership is to assess the quality of phosphatic ore for the manufacture of lithium ferro (iron) phosphate (LFP) batteries.

Petrographic and mineralogic data indicate that fluorapatite is the primary ore mineral, and the host rock is gabbronorite. Gabbronorites are primarily composed of plagioclase (andesine – $An_{42.9\text{-}47.4}$), orthopyroxene (enstatite - $En_{61.2\text{-}68.1}$), and clinopyroxene (diopside- $Wo_{45.6\text{-}46.7}$). In the LSJA, fluorapatite crystals are associated with ilmenite and magnetite crystals, suggesting that the major phase of apatite crystallization was accompanied by the precipitation of these oxide minerals.

After beneficiation, the fluorapatite concentrate has a similar P_2O_5 concentration (40.5-41.2 wt.%) to that of *in situ* fluorapatite crystals in the gabbronorite (41.3-41.8 wt.%) indicating a high P_2O_5 recovery from the host rock. The SiO_2 concentration of the concentrate is 0.93 wt.%. The Cl and F contents of the concentrate are between 800 and 873 ppm and 2.98 and 3.12 wt.%, respectively. The concentrations of other trace metals (Fe, Al, Mg, Ti, Na, Sr, As, Cd, Th, U, and Pb) in the phosphate concentrate range between 0.9 and 5100 ppm and are therefore significantly lower than those in sedimentary phosphate ores.

Enriched concentrations of high-quality apatite and low contents of deleterious trace metals make the Lac à l'Orignal deposit an attractive ESG (environmental, social, and governance)-compliant source of North American P for the LFP battery industry. During phosphoric acid production from beneficiated apatite concentrate, these low trace element concentrations may produce phosphogypsum that can be recycled into plaster and wallboard. Further metallurgical testing may demonstrate that ilmenite and magnetite could be important saleable by-products for Ti and Fe.

TABLE OF CONTENTS

1. Introduction 4

2. Objectives and deliverables 4

3. Background 6

4. Location 6

5. Regional geology 6

6. Sampling 12

7. Methods 12

8. Results

    8.1. Mineralogy and mineral chemistry of Lac à l'Orignal gabbronorite 14
    8.2. Rare earth elements (REE) of apatite and silicate minerals 37
    8.3. Chemistry of Lac à l'Orignal apatite concentrate 40

9. Discussion

    9.1. Variability of concentration data and analytical techniques 44
    9.2. Significance of apatite halogen (F and Cl) content 45
    9.3. Apatite of the Lac à l'Orignal deposit as an ESG-compliant source of P 48
    9.4. Ilmenite and magnetite as secondary commodities 48
    9.5. Mineral paragenesis and timing of apatite crystallization 50

10. Conclusions 51

11. References 52

1. Introduction

The push by developed countries to decarbonize the transport and energy sectors underscores the need for cheaper and more reliable rechargeable batteries for the electric vehicle (EV) market (Spears et al., 2022, Xu et al., 2020). First Phosphate is the only company developing greenfield phosphate deposits to source phosphate for the lithium iron phosphate (LFP; $LiFePO_4$) battery industry. Over 20 years of research have shown that LFP batteries are ideal as a replacement for current lithium-ion batteries because of their higher cycling performance, thermal stability, and superior safety (Padhi et al., 1997; Ye et al., 2018; Ahsan et al., 2021). Other promising variants of the LFP battery contain metals in combination with iron such as manganese (Ling et al., 2021). Because phosphate forms the backbone of the LFP cathode, the ability to acquire a stable and ESG-compliant source of phosphorus is critical as the world transitions to clean energy.

The demand for phosphorus by the growing battery industry is concerning because most of the global production is used for the manufacture of fertilizer (85%) and animal feed (10%; Spears et al., 2022). Governments around the world are acutely aware of this conflict between food security and the supply of phosphorus for LFP battery production. Consequently, many jurisdictions (European Union, Ontario in Canada, and Korea) list phosphate rock and phosphorus as critical raw materials with a high supply risk (European Commission, 2020; Government of Ontario, 2022). First Phosphate is uniquely positioned to alleviate this bottleneck in the supply chain because its Lac à l'Orignal deposit in Québec, Canada (Fig. 1), is a potentially large source of igneous phosphate without environmentally deleterious trace elements that plague many sedimentary phosphatic ores (e.g., Pufahl and Groat, 2017 and references therein).

The purpose of this report is to characterize the nature of First Phosphate's Lac à l'Orignal deposit, which is part of the Lac-Saint-Jean Anorthosite (LSJA) Complex (Fig 1; Higgins et al., 2002; Grant, 2020). The LSJA is the world's largest anorthosite and is a potential long-lived source of phosphorus. Interpretations based on detailed mineralogic, petrologic, and geochemical results reported herein, assess the Lac à l'Orignal deposit as a clean source of North American phosphate for LFP battery production.

2. Objectives and deliverables

Anorthosites from Lac à l'Orignal, Vanel, and Mirepoix are part of the Lac-Saint-Jean Anorthosite (LSJA) Complex. The LSJA Complex is in south-central Quebec, ~300 km north-northeast of Québec City. The complex occurs in the Grenville Structural Province and was emplaced in multiple stages over a 170-million-year period starting 1.1 billion years ago.

The detailed geological nature of the LSJA in the Lac à l'Orignal, Vanel, and Mirepoix properties is unknown. The primary objective of collaborative research is to provide critical new information on the mineralogy and geochemistry of the LSJA to fully assess its character and concentration of phosphate in the Lac à l'Orignal area. This information is essential when making decisions regarding site feasibility, and if economic, how to cost-effectively extract ore under the ESG agenda with the lowest possible carbon footprint.

Fig. 1. Location map showing the Lac à l'Orignal deposit within Quebec in Canada.

Our collaborative research will yield the following key deliverables:

1) Literature review of the geology of anorthosite-hosted phosphate deposits and downstream processes related to LFP battery manufacture.

2) Detailed mineralogy and geochemistry of the Lac à l'Orignal deposit to develop a deposit paragenesis. This paragenesis is the foundation for enhanced interpretative tools that may be used for identifying zones of high-grade phosphate in the LSJA.

3) Publication of research results in a high-impact, peer-reviewed paper, which will help establish First Phosphate as a global leader in the LFP battery supply chain and green energy.

3. Background

Although enormous reserves of phosphate rock exist (68.8 Bt; Pufahl and Groat, 2017), only a small portion is ideally suited for LFP battery production. The raw material for cathode manufacture is generally constrained by the supply of pure phosphoric acid with low trace element concentrations (BM Review, 2022). Our research shows that phosphatic ores derived from anorthosites (< 3 ppm of Cd, Pb, U, and Th) may be the best source to produce phosphoric acid with low levels of deleterious trace elements (Table 1).

Most of the estimated world phosphate reserves are from sedimentary rocks (~95%) that generally contain high trace element concentrations and therefore, are less desirable for LFP battery production (Table 1; Pufahl and Groat, 2017). China, Morocco, and the USA are the top producers of sedimentary-hosted phosphate (USGS 2022). Only a small portion of phosphate (~5%) is derived from igneous rocks (Pufahl and Groat, 2017), most of which is hosted in carbonatites that are mined in Russia and South Africa (El Bamiki et al., 2021).

4. Location

The Lac à l'Orignal deposit is located ~300 km north-northeast of Québec City, Québec (Fig. 2) at longitude 70° 34' 41" W and latitude 49° 04' 28" N (UTM NAD83 Zone 19N coordinates: 384,750 m E and 5,436,930 m N). The deposit is located on NTS sheet 22E02 (P & E Mining Consultants Inc, 2022).

5. Regional geology

The Lac à l'Orignal deposit is part of the Lac-Saint-Jean Anorthosite (LSJA) Complex (Fig. 3). The LSJA Complex occurs in the central part of the Grenville Structural Province (Fig. 2; Higgins and Breemen, 1992). The Grenville Structural Province is ~1600 km long and ~350 km

Table 1. Comparison of average chemistry between sedimentary and igneous (carbonatite and anorthosite) phosphate source rocks. First Phosphates deposits are included for comparison (prepared by C.F. Pufahl for First Phosphate).

	Deposit type**			First Phosphate Quebec Anorthosites		
	Sedimentary	Igneous		Lac à l'Orignal	Mirepoix	Lamarche*
		Carbonatite	Anorthosite			
	average (wt.%)			average (wt.%)		
P_2O_5	29.6	5.37	6.89	6.11	5.58	11.6
Al_2O_3	1.20	3.87	10.1	12.7	9.86	3.82
CaO	45.2	31.8	8.82	11.9	10.5	13.6
FeO	0.18	1.11	-	-	-	-
Fe_2O_3	1.06	3.70	29.1	22.4	27.0	37.8
K_2O	0.33	0.70	0.46	0.59	0.42	0.03
MnO	0.07	0.16	0.22	0.16	0.18	0.33
Na_2O	0.65	0.68	1.73	2.34	1.75	0.45
SiO_2	11.2	5.83	27.4	34.5	30.6	16.7
TiO_2	0.14	0.29	7.97	3.73	6.38	6.78
	(ppm)			(ppm)		
Ba	211	11000	429	578	416	-
Co	11.3	17.0	74.4	66.1	70.0	60.4
Cd	21.0	2.0	2.77	<0.5	0.02	8.3
Cr	160	32.5	294	55.6	86.7	-
La	126	567	31.6	41.0	40.0	40.2
Ni	51.5	40.7	105	21.3	152	0
Pb	90.7	16.0	2.13	<5	<2	0
Rb	16.1	47.6	22.9	4.13	-	54.8
Sr	1270	5630	624	1000	787	-
Th	9.0	43.9	0.69	0.36	-	2.04
Ti	1194	5900	-	-	-	-
U	73.6	38.1	0.29	0.13	-	0.68
V	124	45.0	539	340	252	-
Zr	88.2	323	32.1	79.3	<1	29.8
Cl	378	129	-	-	-	-
F	649	2.03	-	-	-	-
* Analysis from surface grab samples.						

**Data are from Alves (2008), de Oliveira and Imbernon (1998), Berger et al (2009), Cruz et al (1976), El Bamiki et al (2021), Fourie and De Jager (1986), Mikhailova et al (2016), O'Brien et al (2015), Pufahl and Groat, (2017), Rocha et al (2012), Traversa et al (2001), and Verhulst et al (2000).

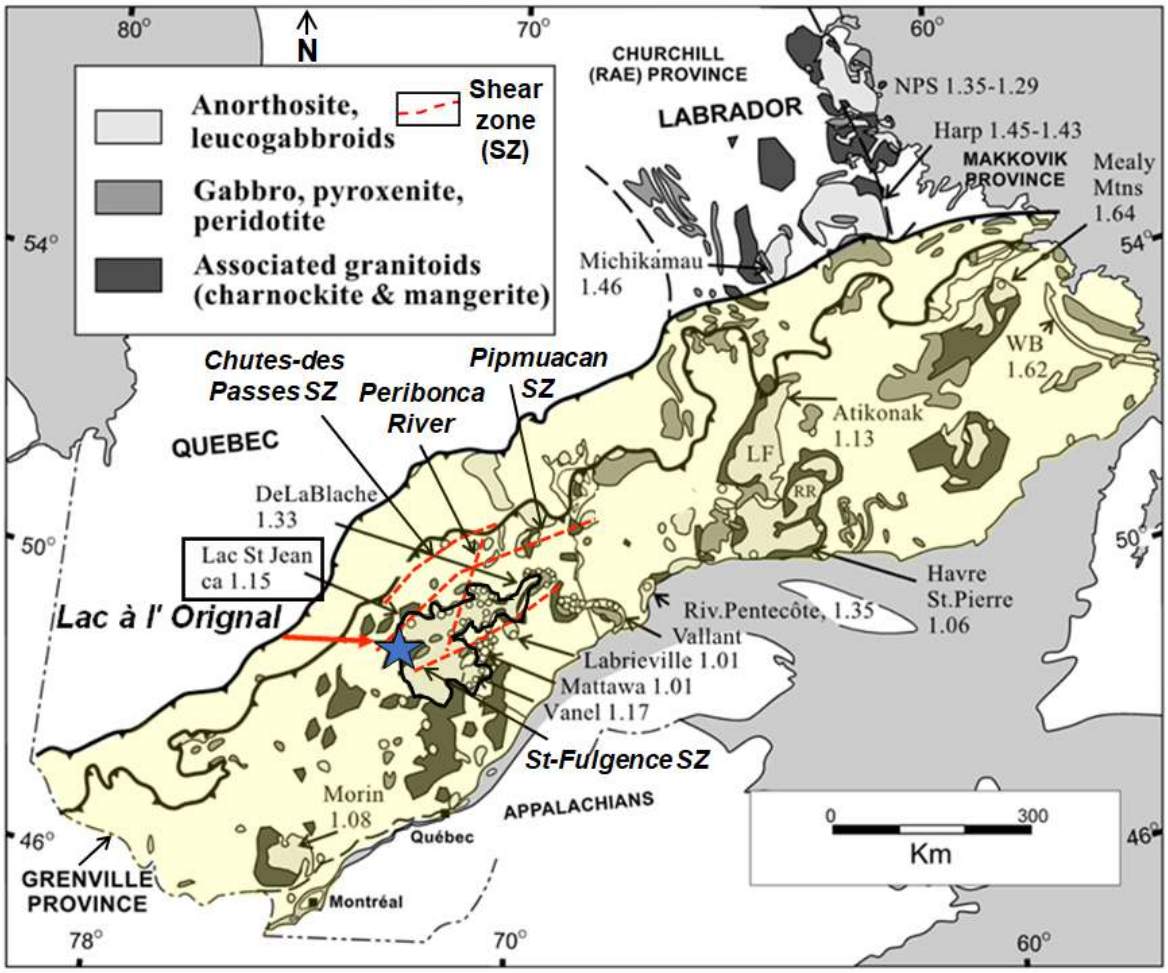

Fig. 2. Location map showing anorthosite bodies and the Lac à l'Orignal deposit within the Grenville Province in Canada. The ages of the anorthosite bodies are also shown (in billion years). WB=White Bear Arm anorthosite, LF=Lac Fournier lobe, RR=rivière Romaine lobe (modified after Bédard, 2009; Higgins et al., 2002).

wide Mesoproterozoic orogenic belt along the southeastern margin of the Canadian Shield (Fig. 2). A prominent feature of the province is that it contains numerous anorthosite massifs and anorthosite-mangerite-charnockite-granite (AMCG) suites, including the LSJA Complex (Hébert et al., 2005).

The LSJA Complex is the largest anorthosite body in the world (Higgins et al., 2002). It consists of a complex assemblage of intrusive anorthosite plutons that are difficult to differentiate based on field relationships and mineralogy. Less abundant intrusive rocks include leuconorite, leucotroctolite, norite, olivine-bearing gabbro, gabbro, pyroxenite, peridotite, dunite, nelsonite, magnetitite, and rare charnockite–mangerite units (Hébert et al., 2005). All are composed of plagioclase with variable amounts of pyroxene and olivine (Higgins et al., 2002). Plagioclase is primarily of the andesine and labradorite varieties (An_{45}- An_{60}; Higgins and Breemen, 1992). The plagioclase ranges in size from millimetric granoblastic crystals in deformed rocks to megacrysts of up to 70 cm long in less deformed rocks. Aluminum-rich orthopyroxene megacrysts are also locally abundant (Higgins and Breemen, 1992).

The anorthosites of the LSJA Complex are interpreted to have intruded in multiple phases over ~170 million years starting at 1160 million years ago (Higgins et al., 2002). The host rocks are the Chicoutimi Gneiss Complex (~1530 million years old), Saguenay Gneiss Complex (~ 1506 million years old), the Hulot Complex (~1434 million years old), the Cap à l'Est Gneiss Complex, and the Cyriac Rapakivi Granite (~1393 to 1383 Ma million years old; Higgins and Breemen, 1996; Hébert et al., 2005). The U-Pb analyses of zircon and baddeleyite from the south-central and southeastern parts of the LSJA Complex provide an igneous crystallization age ranging from 1157 to 1142 million years ago (Higgins et al., 2002). The eastern border of the Complex (Vanel Complex) is of similar age and crystallized between 1180 and 1160 million years ago (Bédard, 2009). Two small leucogabbros dated 1076 million years old confirm a younger episode of igneous activity. Other younger intrusions record periods of granitoid emplacement at 1028 and 988 million years ago during the latter stages of the Grenville Orogeny (Higgins et al., 2002). These ages when considered in the context of all geochronological data from the LSJA Complex region define three periods of magmatism recording a complex and protracted emplacement history. The first period occurred between 1160 and 1140 million years ago. The second was from 1082 to 1050 million years ago, and the third was between 1020 and 1000 million years ago (Higgins and Breemen, 1996). Although the emplacement age of First Phosphate's Lac à l'Orignal deposit is not well constrained, it is thought to have intruded during either the second or third events (Grant, 2020).

At least three major northeast-oriented sets of shear or deformation zones (Chutes-des Passes, Pipmuacan, and St-Fulgence shear or deformation zones) crosscut the LSJA Complex (Fig. 2 and 3). The Peribonca River follows a fourth set, which is oriented north-north-east (Fig. 2). Two large mafic dikes (Lac Chabot and Bégin megadikes) are also oriented north-northeast and show evidence of sinistral movement (Higgins et al., 2002). The fifth set of faults oriented northwest postdates the northeast-oriented shear zones and the two mafic dykes (Higgins et al., 2002).

Solid-state deformation of the LSJA Complex was extremely heterogeneous. Some plutons are undeformed, whereas others have transformed to grey gneiss. Syn-emplacement deformation fabrics and alteration features produced by contact metamorphism from later anorthosite plutons are also common (Higgins and Breemen, 1992).

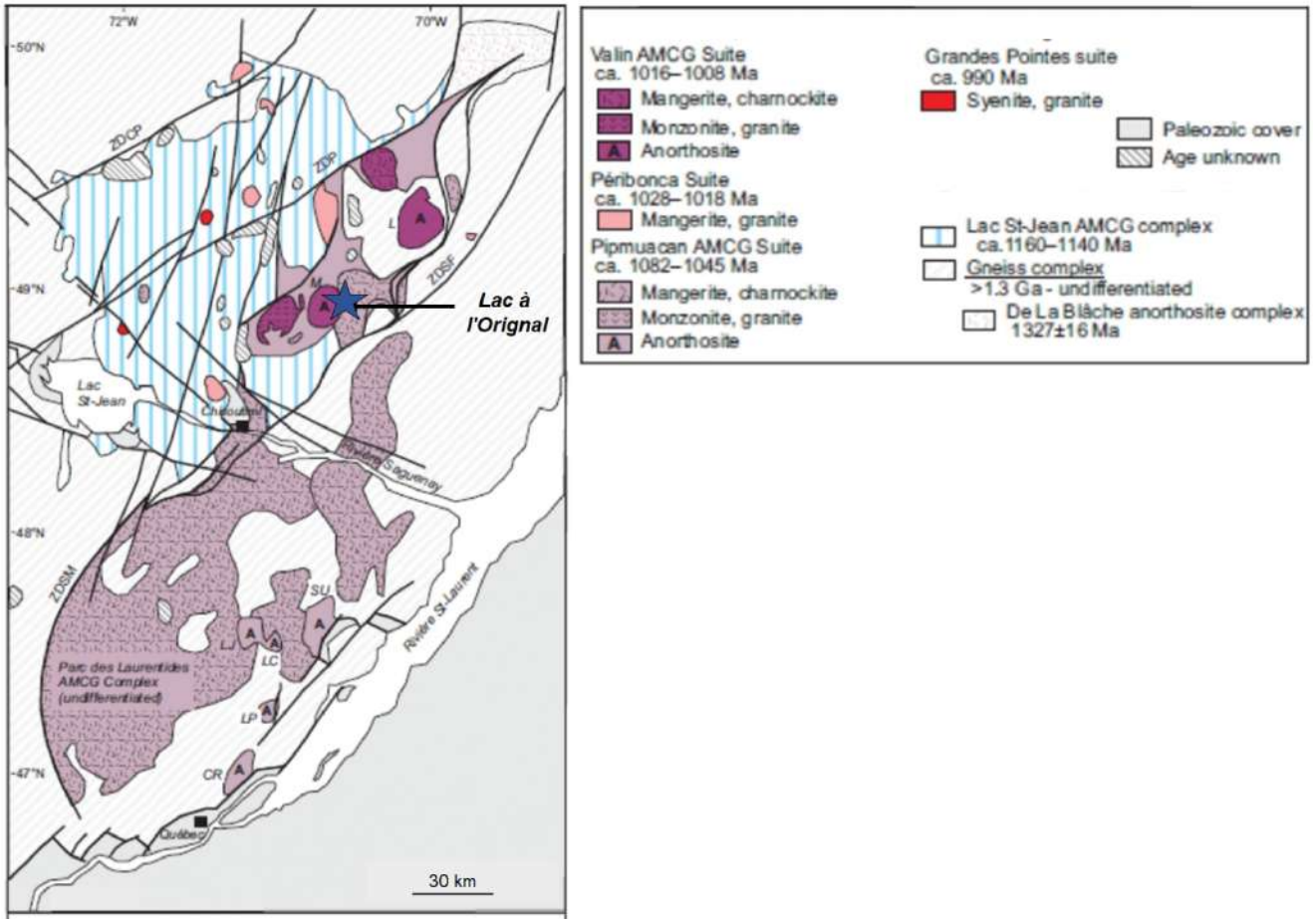

Fig. 3. Geological map of the Lac-Saint-Jean Anorthosite (LSJA) Complex showing the location of the Lac à l'Orignal deposit (modified after Hébert et al., 2005; Grant, 2020). Abbreviations: ZDCP, ZDP, ZDSF, and ZDSM represent Chute des Passes, Pipmuacan, St. Fulgence, and St. Maurice deformation zones, respectively; CR-Château Richer, L-Labriville, LC-Lac Chaudière, LJ-Lac à Jack, LP-Lac Piché, M-Mattawa, SU-St. Urbain (figure from Grant, 2020).

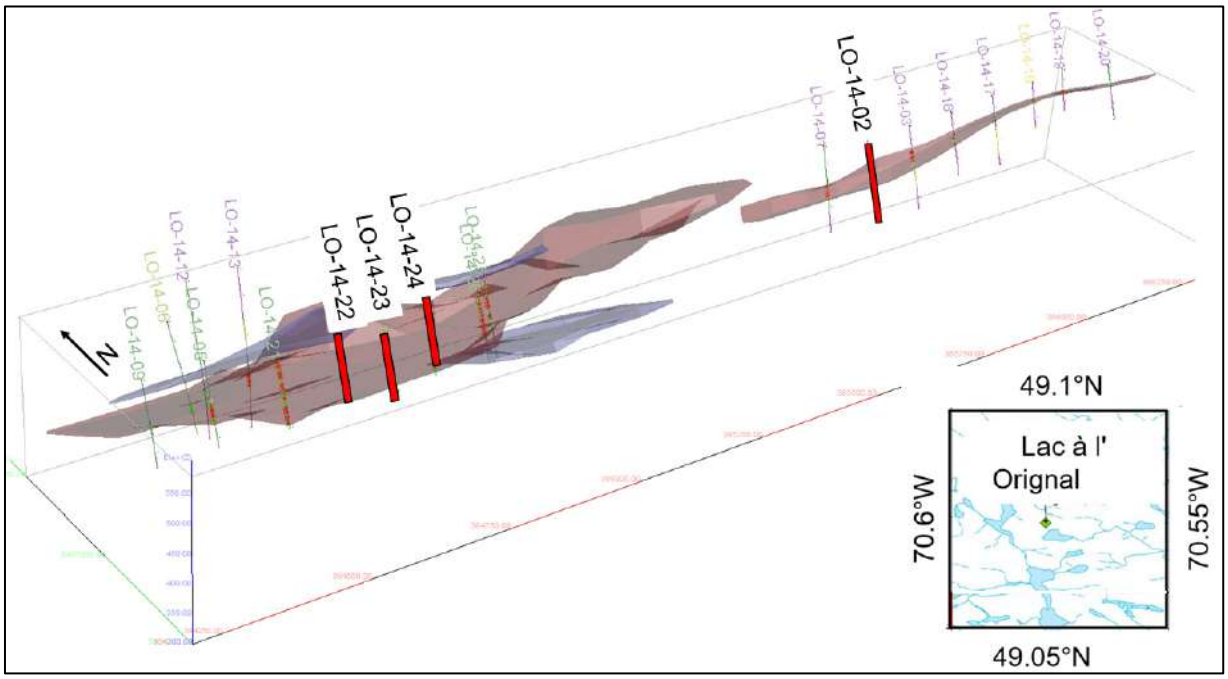

Fig. 4. Drill hole distributions within the Lac à l'Orignal deposit. Sampled drill cores are in red. Inset shows the location of the Lac à l'Orignal deposit (figure prepared by P & E Mining Consultants Inc.).

6. Sampling

A total of 25 core samples were collected from ore zones from drill hole LO-14-22 (four samples), LO-14-23 (nine samples), LO-14-24 (five samples), and LO-14-02 (seven samples, Table 2). The samples were cut into halves and then quarters using a rock saw at the Department of Geology and Geological Engineering, Queen's University. Samples were used for petrographic, X-ray diffraction (XRD), scanning electron microscopy (SEM), electron probe micro analysis (EPMA), and laser ablation inductively coupled plasma mass spectrometry (LA-ICP-MS) analysis (Table 2).

7. Methods

A total of 35 polished thin sections were prepared from the 25 core samples in the Queen's Facility for Isotope Research (QFIR). The corresponding thin section billets (rock slices used to prepare thin sections) were powdered in a ring mill for subsequent analyses (Table 2).

The textural relationships of minerals were investigated in thin sections under transmitted and reflected light using a Nikon eclipse LV 100N microscope. The mineralogy was confirmed using powder XRD analysis on a Malvern Panalytical Empyrean Diffractometer with repeated continuous scans from angles of 5° to 120° using a Co X-ray source (λ=1.79Å). Two internal standards for XRD analysis were prepared from in-house plagioclase, enstatite, augite, hornblende, and fluorapatite. The minerals were powdered separately and mixed at different proportions for preparing the internal standards. The samples were analyzed with duplicates and internal standards. Basic mineral identification was conducted in Highscore Pro 4.9 software using the International Center for Diffraction Data PDF-4+ 2022 database. Mineral abundances were calculated using Rietveld refinement.

Each polished thin section was also analyzed with the FEI Quanta 650 FEG ESEM (ESEM) utilizing the Mineral Liberation Analysis (MLA) to produce high-resolution images of the textural relationships between ore and gangue minerals as well as provide an independent estimate of modal abundance. Samples were measured under a low vacuum at a chamber pressure of 0.45 torr. Energy-dispersive X-ray spectroscopy (EDS) was performed with two Bruker Nano Dual X-Flash detectors, using an accelerating voltage of 25kV and a working distance of 12 mm. Each sample was analyzed with a closely spaced grid of X-ray measurements overlaying a BSE image.

In situ mineral compositions (SiO_2, Al_2O_3, TiO_2, Cr_2O_3, FeO, Fe_2O_3, MnO, MgO, CaO Na_2O, K_2O, P_2O_5, F, and Cl) were determined on 10 polished thin sections (two thin sections from LO-14-22; two thin sections from LO-14-23; four thin sections from LO-14-24; two thin sections from LO-14-02; Table 2) using a JEOL JXA-8230 electron microprobe. The analyses in EPMA (electron probe micro analyzer) used an accelerating voltage of 15 kV, a beam current of 20nA, a beam diameter of 5–10μm, and a counting time of 10s. Natural standards from the Smithsonian Institute were used for the analysis of all phases. The reported data represent an average of three or more analyses of each grain and at least three grains from different parts of each thin section. In the case of apatites, crystals with prismatic section parallel to the c-axis were identified under a petrographic microscope, and mineral compositions were analyzed from those crystals.

Table 2. Core samples with depths in the four drill holes investigated in this study. Analysis type is also included.

Serial no	Depth (m)	Petrographic thin section	XRD	SEM (MLA)	EPMA	LA-ICP-MS
Drill hole LO-14-22						
1	66-67.5	2	2	2	1	
2	75-76.5	2	2	2	1	
3	93-94.5	1	1	1		
4	100.5-102	2	2	2		
Drill hole LO-14-23						
5	22.5-22.7	1	1	1		
6	24-25.5A	2	2	2		
7	27-28.5	2	2	2		
8	33-34.5	2	2	2	1	1
9	40.5-42	1	1	1		
10	52	1	1	1		
11	61.5-63	1	1	1		
12	96-97.5	1	1	1	1	1
13	106.9-107.1	2	2	2		
Drill hole LO-14-24						
14	31.4-31.6	2	2	2	1	1
15	39-40.5	1	1	1	1	1
16	70.5-72	1	1	1	1	1
17	88.5-90	1	1	1		
18	105.4-105.6	1	1	1	1	1
Drill hole LO-14-02						
19	35.9-36.1	1	1	1		
20	57-58.5	2	2	2		
21	64.5-66	1	1	1	1	1
22	73.5-75	1	1	1		
23	78-79.5	1	1	1	1	
24	85.5-87	2	2	2		
25	98.3-98.5	1	1	1		
	Total analysis	***35***	***35***	***35***	***10***	***7***

A trace element is an element that is present in a rock or mineral in concentrations of less than 0.1 wt% or 1000 ppm (Rollinson, 2014). Depending on mineral structure one element can be present as a major element in one mineral and the same element can be present as a trace element in another mineral. The trace element composition (Mg, Ti, V, Cu, Zn, As, Sr, Cd, Sn, Sb, Cs, Ba, La, Ce, Pr, Nd, Sm, Eu, Gd, Tb, Dy, Ho, Er, Tm, Yb, Lu, Pb, Th, and U) of *in situ* minerals in seven thin sections (two thin sections from LO-14-23; four thin sections from LO-14-24; one thin section from LO-14-02; Table 2) were analyzed using a NewWave/ESI 193-nm ArF Excimer laser system coupled to a ThermoScientific X Series 2® quadrupole ICP-MS (inductively coupled plasma-mass spectrometry). The laser reference glass standards GSE-1G, NIST614, NIST612, and NIST610 were used, while Durango and Tioga apatite were used as matrix-matched reference materials. Spots on standards and reference materials were ablated before and after each set of samples and preferred values sourced from GeoReM were used for data reduction (Jochum et al., 2005, 2011). Before each spot analysis, a gas blank was measured for 20s to establish background values. A beam diameter of 35µm with a laser repetition rate of 10 Hz and a scan speed of 15 or 7 µm/s were used. Laser energy was checked daily, and fluence was between 7.6 and 7.8 J/cm2. When choosing sites to ablate, care was taken to avoid visible inclusions in the crystals. Data were reduced using the Iolite 4 software (Woodhead et al., 2007; Paton et al., 2011). Variations in element concentrations were reported as either ranges or standard deviations (±1σ).

In situ mineral compositions (e.g., Si, Al, Fe, Mn, Mg, Ca, Na, K, P, F, and Cl) were also determined by SGS, Lakefield using an SEM with a dedicated energy dispersive spectrometer (EDS; SGS, 2022a). As part of SGS' metallurgical study, apatite crystals were separated from the host rock using magnetic separation and flotation (SGS, 2022b). Initially, ground sample (P_{80} of 120 µm; P_{80} = particle size at which 80% of the material will pass when screened) was passed through a low-intensity magnetic separator (LIMS) to remove magnetite. This magnetitic concentrate was then passed through a Davis tube to further separate magnetically susceptible minerals from non-magnetic minerals. The non-magnetic fraction underwent seven flotation tests to recover apatite and produce an apatite concentrate (P & E Mining Consultants Inc, 2022). Fractions of this apatite concentrate were analyzed for their chemical composition by Actlabs, Prayon, and Nutrien to authenticate the concentration of recovered apatite.

8. Results

8.1. Mineralogy and mineral chemistry of Lac à l'Orignal gabbronorite

The major rock type composing the LSJA Complex in the Lac à l'Orignal deposit is a gabbronorite with plagioclase (~8-95%), orthopyroxene (~0-35%), clinopyroxene (~0-11%), amphibole (~0-8%), biotite (~0-18%), apatite (0-19%), ilmenite (0-10%), and magnetite (1-21%; Table 3). Al-spinel and sulfide minerals are present as accessory minerals (< 3%). Most core samples exhibit alternating phaneritic leucocratic (light-colored) and melanocratic (dark-colored) layers. The leucocratic layers are composed almost entirely of plagioclase and the melanocratic layers are formed of mafic (pyroxene, biotite) and oxide (ilmenite and magnetite) minerals. The phosphatic ore mineral is fluorapatite. True anorthosite with > 90% of plagioclase was also identified from this deposit. Anorthosite, however, contains an insignificant amount of apatite (< 5%).

Table 3. Mineral distributions of rocks from the Lac à l'Orignal deposit investigated in this study.

Sample name	Plagioclase	Orthopyroxene	Clinopyroxene	Ilmenite	Hematite	Magnetite	Biotite	Amphibole	Apatite
Drill hole LO-14-22									
LO 29-30	29.2	24.5	8.9	6.0	0.1	14.2	3.9	0.6	12.7
LO 34-35	56.7	16.4	2.1	5.1	0.1	11.4	0.8	0.6	6.8
LO 33	44.5	19.7	1.7	3.4	0.4	7.7	3.2	0.0	19.5
LO 31-32	61.3	12.6	3.6	3.4	0.1	12.5	3.4	0.0	3.1
Drill hole LO-14-23									
LO 14	75.4	2.0	1.3	2.6	0.6	3.1	2.7	0.0	12.3
LO 15-16	69.2	3.9	3.0	3.5	0.7	5.2	3.4	0.0	11.1
LO 7	41.5	21.6	11.1	4.2	1.6	2.7	1.0	0.0	16.3
LO 9-10	58.4	17.7	2.4	2.3	0.9	4.1	4.4	0.0	9.9
LO 11	30.2	30.2	2.3	7.0	0.8	8.5	4.7	0.0	16.2
LO 19	28.9	24.2	5.5	5.3	0.0	12.7	3.6	5.0	14.8
LO 12A	21.0	33.2	4.1	7.8	0.0	14.5	2.9	2.9	13.7
LO 13B	29.4	24.1	3.1	3.9	0.1	16.7	4.4	0.0	18.3
LO 17-18	72.3	16.7	4.5	1.0	0.4	0.8	2.8	0.0	1.4
Drill hole LO-14-24									
LO 5-6	61.0	0.0	0.4	2.3	3.0	8.6	17.6	0.0	7.0
LO 1B	8.1	35.4	5.9	7.9	0.6	17.5	2.4	7.6	14.5
LO 2C	25.2	27.0	2.9	6.2	0.1	14.9	3.3	2.3	18.1
LO 3B	46.7	18.3	1.8	3.0	0.0	6.1	4.0	0.0	20.1
LO 4	62.5	11.4	4.3	4.5	0.7	10.6	5.0	0.0	0.9
Drill hole LO-14-02									
LO 27	69.6	8.8	3.1	3.8	0.1	6.8	2.5	0.0	5.3
LO 20-21	70.2	8.9	3.5	2.8	0.0	5.5	2.7	0.0	6.3
LO 22C	12.8	30.9	8.6	9.7	0.3	21.4	1.4	0.0	14.8
LO23B	57.2	16.9	2.0	2.1	0.2	3.5	2.4	0.0	15.7
LO24A	39.9	22.4	1.9	5.9	0.7	9.5	3.0	0.0	16.6
LO 25-26	50.7	21.0	2.9	4.4	0.2	6.7	3.7	0.0	10.5
LO 28	94.9	0.0	0.4	0.2	0.2	0.7	3.6	0.0	0.1

* Mineral distribution is an average of two measurents by two techniques, XRD and MLA.

It is important to note that the interpretations of the mineralogical, petrological, and geochemical data are based on a small set of samples of the deposit and the suite of samples may not be truly representative of the entire Lac à l'Orignal deposit. A description of the petrographic and geochemical characteristics of individual minerals composing the Lac à l'Orignal deposit is provided below.

Plagioclase ($NaAlSi_3O_8 – CaAl_2Si_2O_8$): Plagioclase crystals of the gabbronorite are euhedral to subhedral in shape. The crystals range in size from ~ 1 mm to ≥ 10 mm. Equant crystals of plagioclase are common in the gabbronorite (Fig. 5A). Many plagioclase crystals of the gabbronorite contain inclusions of (ortho or clino) pyroxene and oxide minerals (ilmenite or magnetite) (Fig. 5B). In some cases, inclusions of apatite are also observed within plagioclase crystals of the gabbronorite (Fig. 5B).

Large plagioclase crystals (~ 4 mm) associated with small plagioclase crystals (~0.5 mm) occur in the anorthosite (Fig. 5C). Granoblastic texture with plagioclase crystals with serrated crystal boundaries are interpreted to be the consequence of dynamic recrystallization (Fig. 5C). The presence of rare tartan twins within plagioclase crystals indicate that twin boundary migration was also associated with dynamic recrystallization (Fig. 5D). Bent lamellar twinning in plagioclase records deformation.

All plagioclase is andesine with end member compositions of anorthite (42.9-47.4 mol.%), albite (50.4-56.1 mol.%), and orthoclase (1.0-2.5 mol.%). The SiO_2 (56.1-57.0 wt.%) and Al_2O_3 (27.0-27.9 wt.%) contents have very narrow ranges (Table 4).

Common trace elements include Ba (298 ± 115 ppm), Mg (176 ± 75 ppm), Ti (112 ± 88 ppm), Zn (7 ± 3 ppm), Pb (5 ± 1 ppm), Cu (2 ± 0.7 ppm), Sn (2 ± 0.5 ppm), Cd (1.5 ± 0.8 ppm), Sb (0.7 ± 0.6 ppm), V (0.7 ± 0.7 ppm), Cs (0.2 ± 0.1 ppm), Th (0.1 ± 0.1 ppm), and U (0.1 ± 0.1 ppm) (Fig. 6). Sr concentrations (2100 ± 415 ppm) are much higher than all other trace elements (Fig. 6).

Oxide concentrations of Al, Ca, Na, K, and Fe reported by EPMA were also recalculated to elemental concentrations to compare with elemental concentrations analyzed by LA-ICP-MS and SEM (Table 5). Like LA-ICP-MS, SEM-EDS analysis reports concentrations of elements, not concentrations of oxides. Although values are not identical, they are comparable to the same order of magnitude (Fig. 7). Variations in concentrations of Ca analyzed by EPMA and LA-ICP-MS range between 0 and ±20% (Fig. 7). In general, concentrations of elements (Al, Ca, Na, K, and Fe) analyzed by the SEM exhibit wider ranges than those analyzed by EPMA (Table 5).

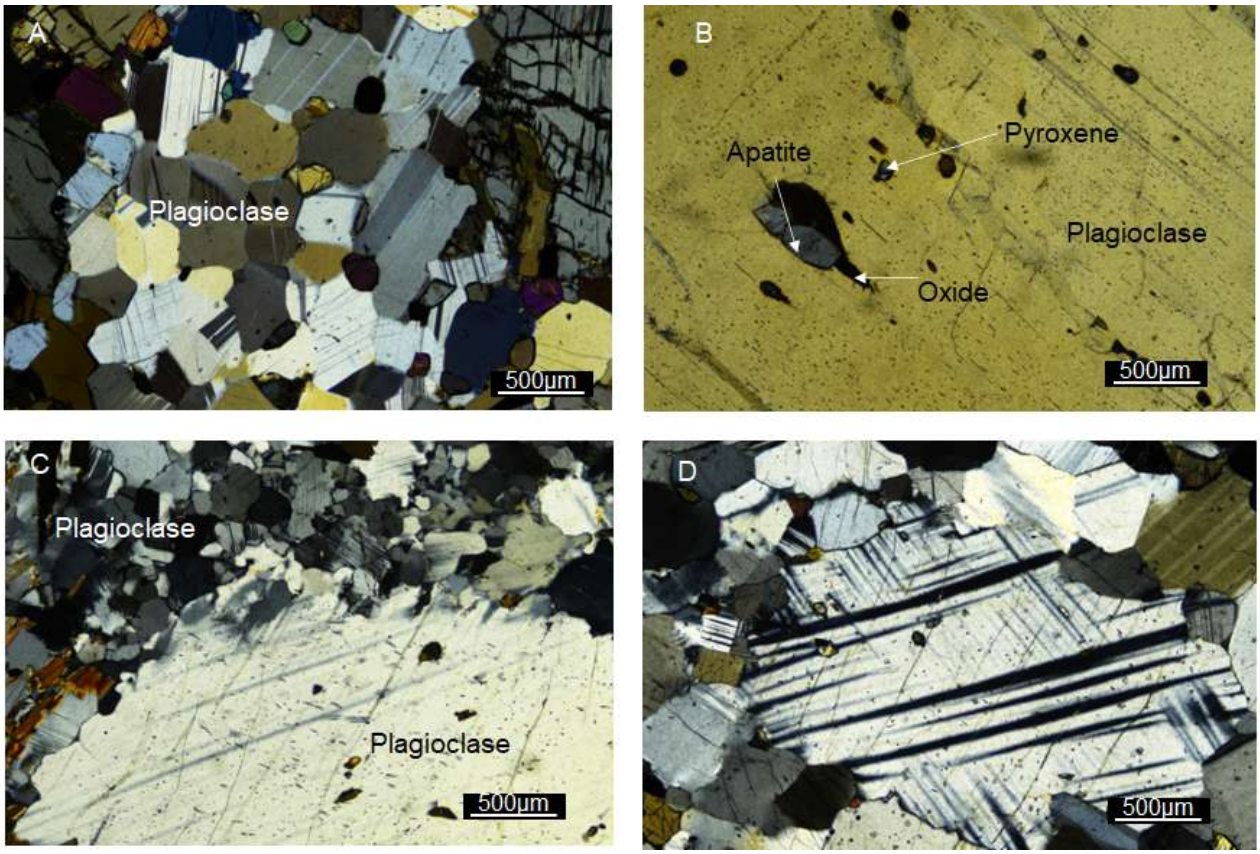

Fig. 5. Textural relationships of plagioclase from the Lac à l'Orignal deposit (cross-polarized transmitted light). (A) Equant crystals of plagioclase composing gabbronorite; (B) pyroxene and apatite inclusions within large plagioclase crystal; (C) Granoblastic texture and plagioclase crystal with serrated crystal in anorthosite; (D) Tartan twinning within plagioclase crystals of anorthosite.

Table 4. Ranges of chemical compositions of minerals of gabbronorites from the Lac à l'Orignal deposit analyzed by EPMA.

	Plagioclase	Orthopyroxene	Clinopyroxene	Amphibole	Biotite	Apatite	ilmenite	Magnetite
	(wt%)							
SiO_2	56.1-57.0	51.1-52.5	50.5-51.2	41.2-41.6	36.6-37.9	0.07-0.22	≤0.01	0.01-0.02
Al_2O_3	27.0-27.9	2.02-2.68	3.92-4.23	13.2-13.8	14.7-15.7		0.01-0.04	0.32-0.45
TiO_2		0.09-0.12	0.51-0.61	1.93-2.98	4.0-5.5		46.2-50.0	0.07-0.25
Cr_2O3		0.0-0.01	0.0-0.01	0.0-0.01	0.0-0.01		≤0.01	0.02-0.12
FeO	0.08-0.22	19.9-23.4	8.1-9.25	10.9-11.7	7.66-13.1		38.4-40.6	31.0-31.3
Fe_2O_3							6.96-12.2	67.6-68.1
MnO		0.48-0.79	0.23-0.32	0.11-0.17	0.02-0.03	0.02-0.05	0.42-0.84	≤0.01
MgO		21.3-24.0	12.8-13.9	12.7-13.5	15.3-19.5		0.75-1.98	0.03-0.11
CaO	8.9-9.74	0.38-0.66	21.2-22.0	11.2-11.7	0.01-0.02	54.7-55.3	0.01-0.03	≤0.01
Na_2O	5.72-6.41	0.01-0.03	0.63-0.74	1.83-2.3	0.04-0.23	0.03-0.16		
K_2O	0.17-0.43		≤0.01	1.02-2.02	9.19-9.73			
P_2O_5						41.3-41.8		
F				0.55-0.74 (5500-7400 ppm)	0.83-1.32 (8300-13200 ppm)	3.66-4.11 (36600-41100 ppm)		
Cl				0.02-0.03 (164-317 ppm)	0.02-0.04 (150-437 ppm)	0.07-0.10 (700-1044 ppm)		
H_2O				1.66-1.76	3.44-3.69	0.02-0.11		
mg#		61.9-68.9	71.1-75.3	65.9-68.5	67.5-81.9			
CaO/P_2O_5						1.31-1.33		
F/Cl				20.5-33.2	23.9-64.3	33.7-52.3		
End members	$An_{42.9-47.4}$ $Ab_{50.4-56.1}$ $Or_{1.0-2.5}$	$En_{61.2-68.1}$ $Fs_{30.7-37.6}$ $Wo_{0.8-1.4}$	$Wo_{45.6-46.7}$ $En_{38.2-40.7}$ $Fs_{13.3-15.5}$					

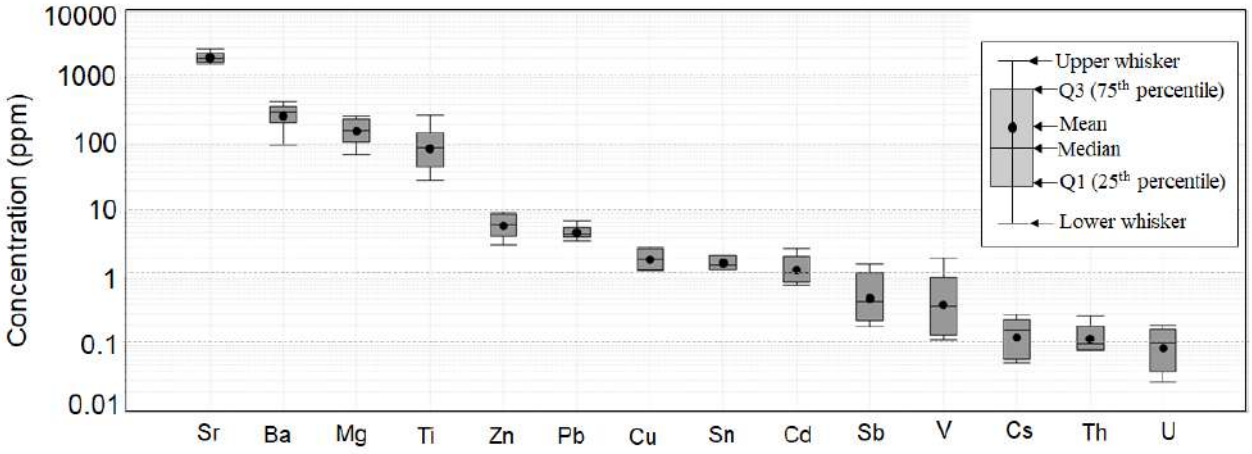

Fig. 6. Concentrations of selected trace elements in plagioclase.

Table 5. Comparison of elemental concentration data obtained by LA-ICP-MS, EPMA, and SEM from selected minerals composing the Lac à l'Orignal deposit.

	LA-ICP-MS (ppm)*	EPMA (ppm)*	SEM (wt. %)
Plagioclase			Reported as feldspar
Al	162000-170000 (16.2-17.0)	143000-148000 (14.3-14.8)	12.7-14.3
Ca	52900-61000 (5.29-6.1)	63300-69500 (6.33-6.95)	4.8-6.9
Na	39200-41800 (3.92-4.18)	42500-47500 (4.25-4.75)	4.0-5.3
K	1100-3200 (0.11-0.32)	1400-3300 (0.14-0.33)	0.2-0.4
Fe	550-1200 (0.06-0.12)	599-1100 (0.06-0.11)	0.3-0.9
Orthopyroxene			Reported as pyroxene
Fe	116600-170000 (11.7-17.0)	154400-181600 (15.4-18.2)	14.6-23.9
Mg	119900-131300 (12.0-13.1)	128000-143300 (12.8-14.3)	5.2-14.3
Al	12100-12960 (12.1-13.0)	12070-14180 (12.1-14.2)	1.0-16.6
Ca	2770-3620 (0.28-0.36)	2700-4060 (0.27-0.41)	0.3-1.5
Mn	4070-4700 (0.41-0.47)	3750-4300 (0.38-0.43)	0.5-0.6
Ti	532-2220 (0.05-0.22)	532-750 (0.05-0.08)	
Na	58-111	100-155	
Cr	5.0-15	15-35	
Apatite			
Ca		390800-394900 (39.1-39.5)	36.9-42.6
P		180200-183500 (18.0-18.4)	18.2-19.6
Si	783-1546 (0.08-0.15)	362-1013 (0.04-0.1)	0.1-1.7
Sr	814-1755	646-1377	
Na	317-797	347-533	
Mn	289-430	184-419	
As	2.0-17	15-51	
F		36600-41100 (3.66-4.11)	4.1-5.9
Cl		700-1044 (0.07-0.1)	0.2-0.4
Ilmenite			
Fe		323000-358400 (32.3-35.8)	19.9-41.7
Ti	188300-350300 (18.8-35.0)	276900-300600 (27.7-30.1)	20.7-34.6
Mg	2831-10200 (0.28-1.02)	4500-11900 (0.45-1.19)	0.4-1.3
Mn	2830-7050 (0.28-0.71)	3250-6500 (0.33-0.65)	0.3-0.8

LA-ICP-MS analysis and EPMA were done at Queen's University and SEM was done at SGS.
* wt% corresponding to ppm value is reported in parenthesis.

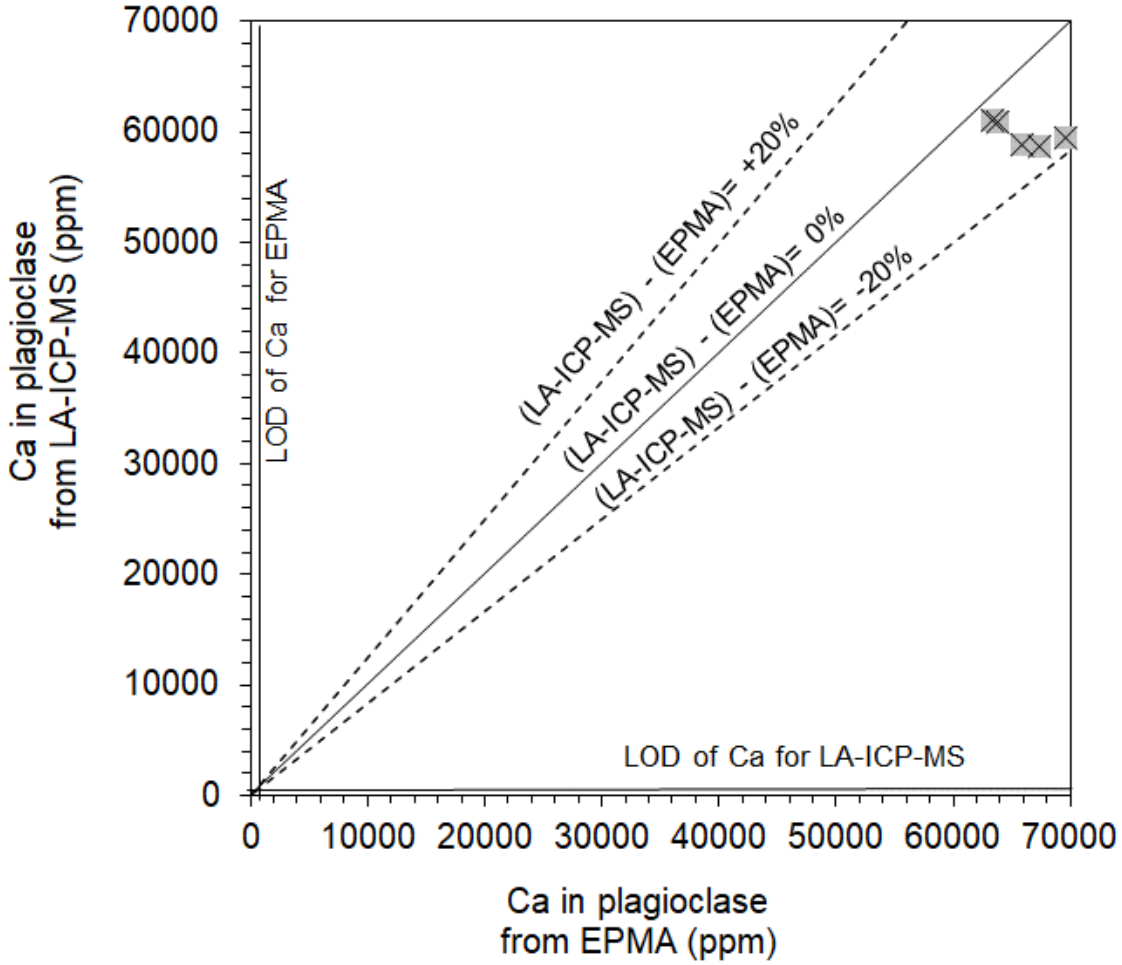

Fig. 7. Comparison of Ca contents of plagioclase analyzed by EPMA and LA-ICP-MS. LOD = lower limit of detection.

Orthopyroxene ($Mg_2Si_2O_6$-$Fe_2Si_2O_6$): Orthopyroxene crystals of the gabbronorite are mostly subhedral and range in size from ~0.1 mm to > 2 mm. Orthopyroxene crystals occur as an intercumulate phase (Fig. 8A and B) and are generally associated with oxide minerals (magnetite and ilmenite) and plagioclase (Fig. 8A and B). Orthopyroxene surrounded by plagioclase produces a poikilitic texture (Fig. 8A), which is a typical texture in gabbronorite. In some cases, corroded crystal boundaries between orthopyroxene and oxide minerals are observed (Fig. 8C). Exsolution of ilmenite and or rutile within orthopyroxene is also observed. This texture is common within larger orthopyroxene crystals (> 1mm, Fig. 8D). Inclusions of apatite and oxide minerals within orthopyroxene crystals are common (Fig. 8E and F).

The orthopyroxene is enstatite-rich with end member compositions of enstatite (61.2-68.1 mol.%), ferrosilite (30.7-37.6 mol.%), and wollastonite (0.8-1.4 mol.%). The Al_2O_3 (2.02-2.68 wt.%), TiO_2 (0.09-0.12 wt.%), Na_2O (0.01-0.03 wt.%), and Cr_2O_3 (≤0.01 wt.%) contents of orthopyroxene are low. The magnesium number (mg# = Mg/ (Mg + Fe^{2+})) of orthopyroxene varies between 61.9 and 68.9 (Table 4). The mg# of mafic silicate minerals is an indicator of stages of magmatic differentiation (Zieg and Wallrich, 2018).

Common trace elements include Ti (893 ± 742 ppm), Zn (644 ± 172 ppm), V (60 ± 17 ppm), As (2.9 ± 1.9 ppm), Cu (2.2 ± 0.7 ppm), Cd (1.3 ± 0.5 ppm), Sr (1.2 ± 0.8 ppm), Ba (1.1 ± 1.3 ppm), Sn (0.7 ± 0.05 ppm), Sb (0.4 ± 0.2 ppm), Pb (0.4 ± 0.38 ppm), Th (0.1 ± 0.08 ppm), Cs (0.1 ± 0.07 ppm), and U (0.1 ± 0.08 ppm; Fig. 9). As in plagioclase, values obtained by LA-ICP-MS, SEM, and EMPA are not identical, but comparable to the same order of magnitude with similar ranges. For example, variations in concentrations of Ca of orthopyroxene analyzed by EPMA and LA-ICP-MS also fall between 0 and ±20% (Fig. 10). Concentrations of Fe, Mg, Al, and Ca of pyroxene (reported as pyroxene) analyzed by SEM, however, exhibit wider ranges than those analyzed by EPMA and LA-ICP-MS (Table 5).

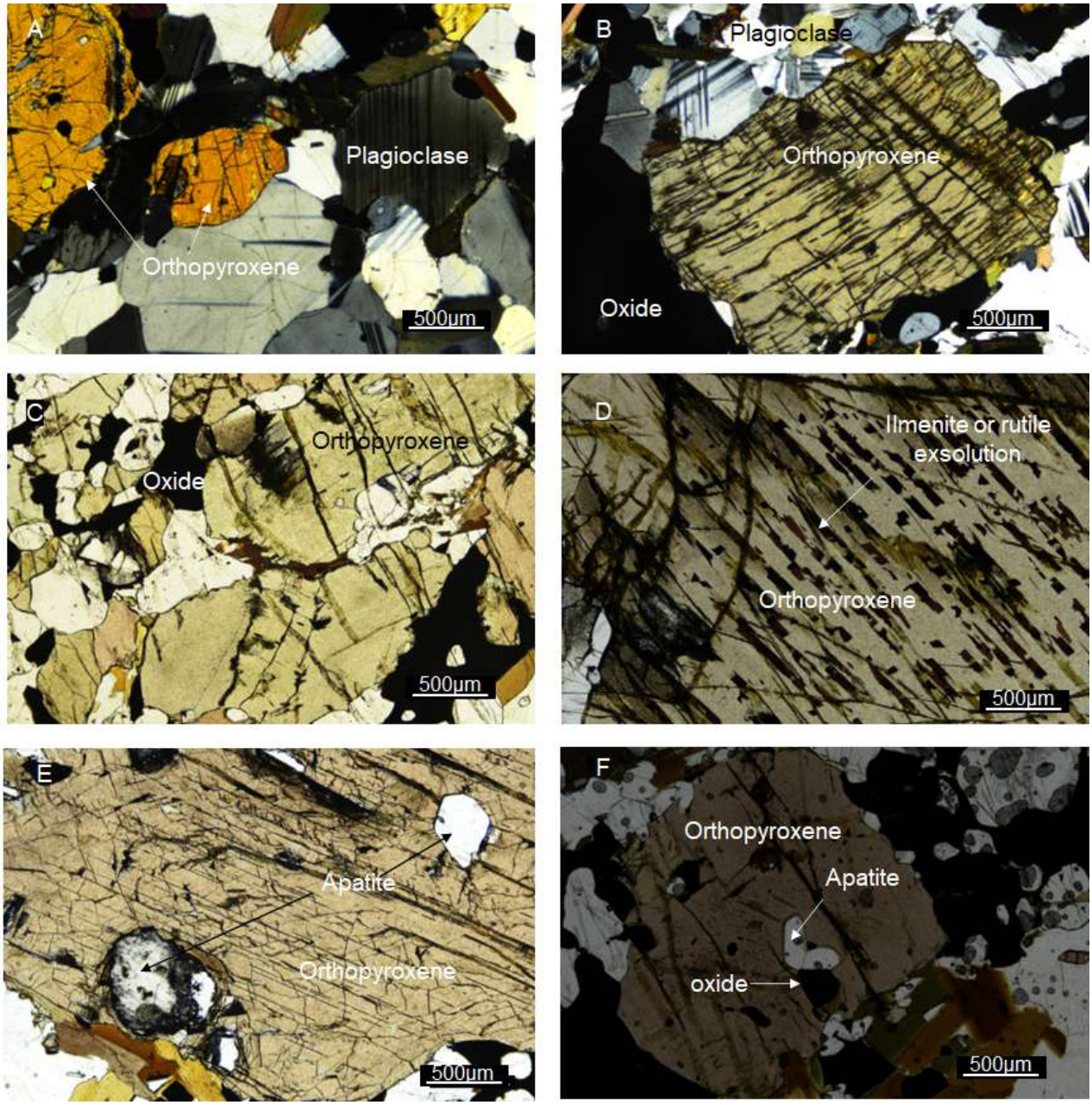

Fig. 8. Textural relationships of orthopyroxene from the Lac à l'Orignal deposit (transmitted light). (A) Orthopyroxene crystals surrounded by plagioclase crystals showing poikilitic texture in gabbronorite (cross-polarized light); (B) Large orthopyroxene crystal surrounded by plagioclase and oxide (ilmenite and magnetite) crystals (cross-polarized light); (C) Corroded crystal boundaries between orthopyroxene and oxide minerals (plane-polarized light); (D) Ilmenite or rutile exsolutions within orthopyroxene crystal (plane-polarized light); (E) and (F) Apatite inclusions within orthopyroxene crystals (plane-polarized light).

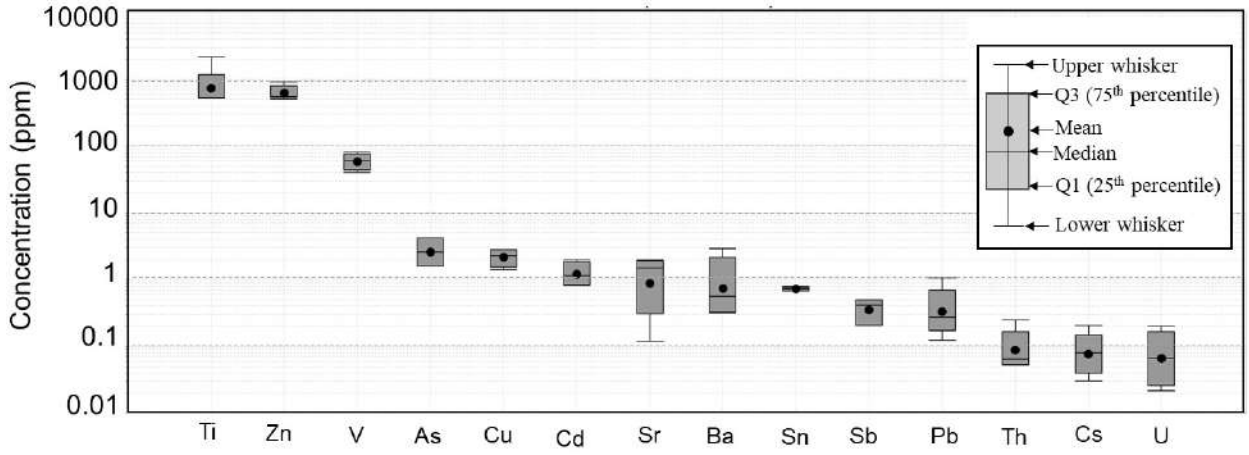

Fig. 9. Concentrations of selected trace elements in orthopyroxene.

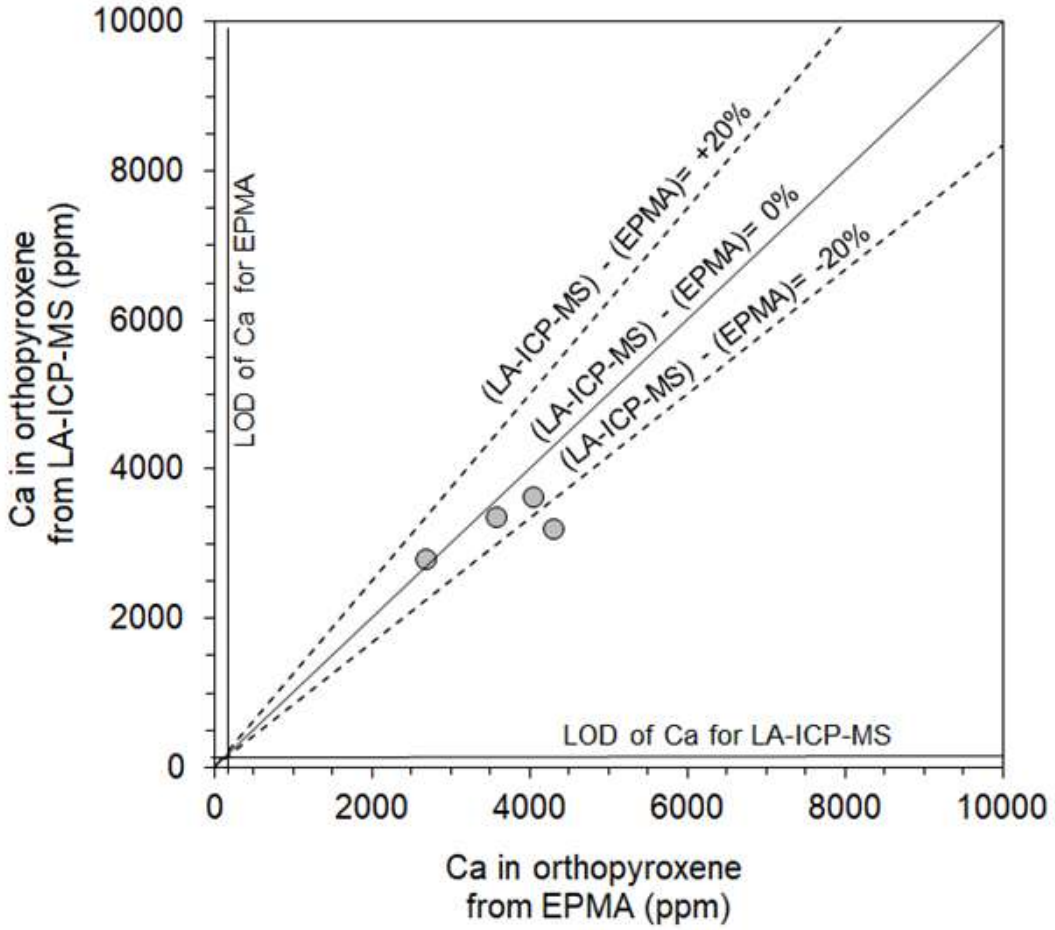

Fig. 10. Comparisons of Ca contents of orthopyroxene analyzed in EPMA and LA-ICP-MS. LOD = lower limit of detection.

Clinopyroxene ($(Ca,Mg,Fe)\ (Mg,Fe)Si_2O_6$): The abundances of clinopyroxene are significantly lower than that of orthopyroxene in the gabbronorite (clinopyroxene/orthopyroxene ratio ~ 0.1 to 0.5). Clinopyroxene crystals, like orthopyroxene, are mostly subhedral. The crystals range in size from ~0.1 mm to > 2 mm and are generally associated with orthopyroxene and plagioclase cumulate (Fig. 11A). Ophitic texture, where a clinopyroxene crystal envelops plagioclase crystals (Fig. 11B) is a locally important texture.

Clinopyroxene is of the diopside variety with end member compositions of wollastonite (45.6-46.7 mol.%), enstatite (38.2-40.7 mol.%), and ferrosilite (13.3-15.5 mol.%). The Al_2O_3 (3.92-4.23 wt.%), Na_2O (0.63-0.74 wt.%), and TiO_2 (0.51-0.61 wt.%) contents of clinopyroxene are higher than those of orthopyroxene, whereas the Cr_2O_3 contents (≤0.01 wt.%) are similar. Finally, the mg# of clinopyroxene (71.1-75.3) is higher than that of orthopyroxene (Table 4).

Amphibole ($(Ca,Na)_2(Mg,Fe,Al)_5(Al,Si)_8O_{22}(OH)_2$): Amphibole crystals are rare, subhedral to anhedral, and associated with clinopyroxene and orthopyroxene (Fig. 12A and B). They range in size from ~0.5 to 1 mm. Conversion of orthopyroxene to amphibole was also observed (Fig. 12B).

Amphibole crystals are pargasite and magnesiohastingsite with a narrow range of mg# (65.9-68.5). The Al_2O_3 (13.2-13.8 wt.%), TiO_2 (1.93-2.98 wt.%), and Na_2O (1.83-2.3 wt.%) contents of amphibole are higher than those of orthopyroxene and clinopyroxene. The Cr_2O_3 contents (≤0.01 wt.%) of amphibole are similar to those of orthopyroxene and clinopyroxene (Table 4). The F and Cl contents of amphiboles are 0.55-0.74 wt.% and 0.02-0.03 wt.%, respectively (Fig. 13). F/Cl ratios range between 20.5 and 33.2 (Table 4).

Biotite ($K(Mg,Fe)_3AlSi_3O_{10}(F,OH)_2$): Biotite is not common (< 5%) in the gabbronorite. High abundances were only observed in sample LO 5-6, which contains ~18% biotite (Table 3). Biotite crystals are tabular, range in size from ~0.2 mm to 2 mm, and are associated with plagioclase and oxide minerals (Fig. 14A and B). They do not show any preferred orientation and are interpreted as an intercumulate phase.

Biotite has a widely variable mg# (67.5-81.9). The Al_2O_3 (14.7-15.7 wt.%), TiO_2 (4.0-5.5 wt.%), and Na_2O (0.04-0.23 wt.%) contents are higher than those of orthopyroxene, clinopyroxene, and amphibole. The F (0.83-1.32 wt.%) contents are also higher than those of amphibole, whereas Cl (0.03-0.04 wt.%) concentrations are similar (Fig. 13 and Table 4). The F/Cl ratios of biotite (23.9-64.3) have a wider range (Table 4).

Trace elements include Na (793 ± 541 ppm), Zn (572 ± 537 ppm), V (272 ± 118 ppm), Rb (249 ± 347 ppm), Sr (29 ± 29 ppm), Cu (5.5 ± 1.7 ppm), Sn (1.9 ± 0.8 ppm), Pb (1.3 ± 0.4 ppm), Cd (0.9 ±1.3 ppm), Cs (1.4 ± 1.9 ppm), Sb (0.2 ± 0.15 ppm), Th (0.1 ± 0.04 ppm), and U (0.05 ± 0.02 ppm; Fig. 15).

The Al_2O_3 versus mg# and TiO_2 versus mg# within orthopyroxene, clinopyroxene, amphibole, and biotite do not show any correlation (Fig. 16). However, Al_2O_3 and TiO_2 contents increase progressively from orthopyroxene, clinopyroxene, amphibole, and biotite (Fig. 16).

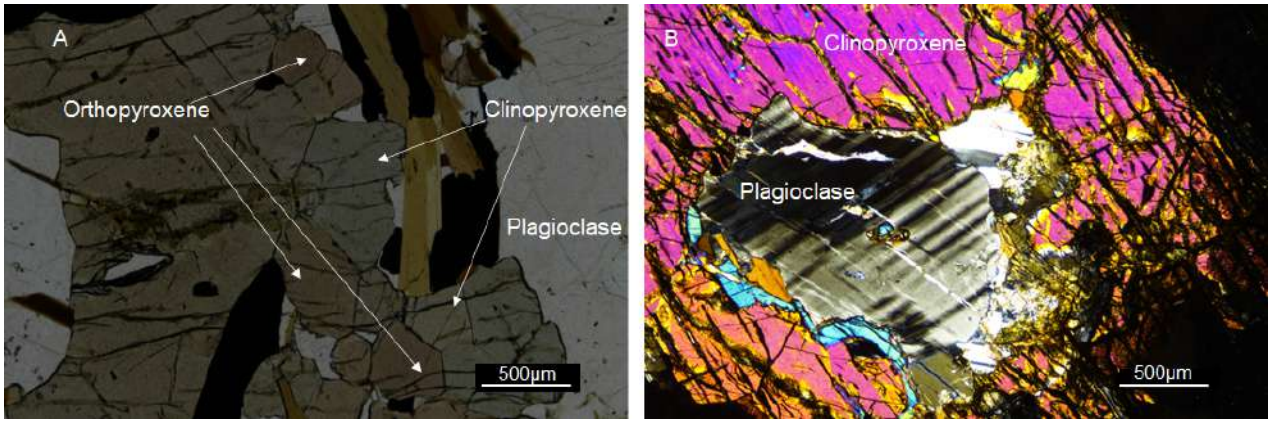

Fig. 11. Textural relationships of clinopyroxene from the Lac à l'Orignal deposit (transmitted light). (A) Clinopyroxene crystals associated with orthopyroxene (plane-polarized light); (B) Large clinopyroxene crystal encloses plagioclase (cross-polarized light).

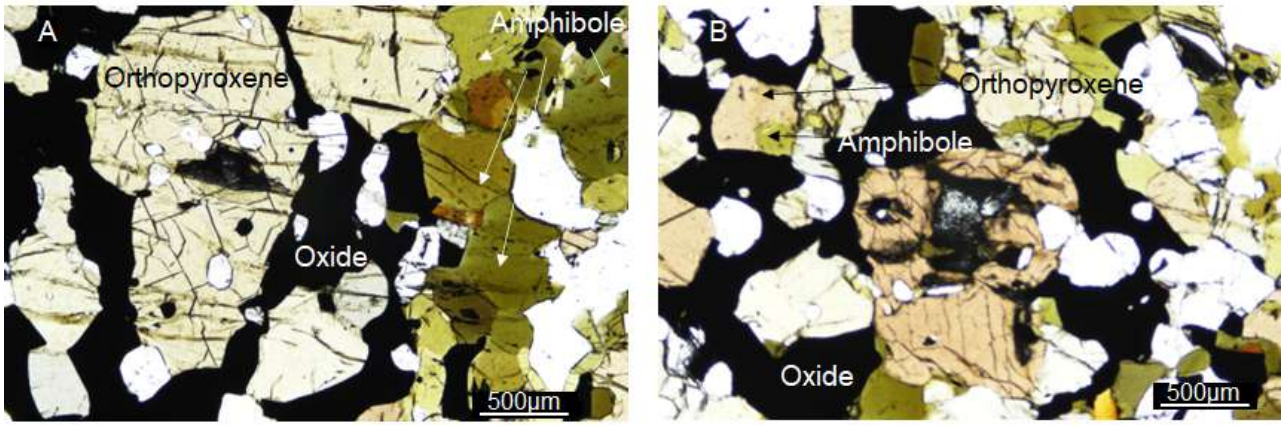

Fig. 12. Textural relationships of amphibole from the Lac à l'Orignal deposit (transmitted light). (A) and (B) Subhedral to anhedral amphibole crystals associated with orthopyroxene crystals (plane-polarized light). The conversion of orthopyroxene to amphibole is shown in B.

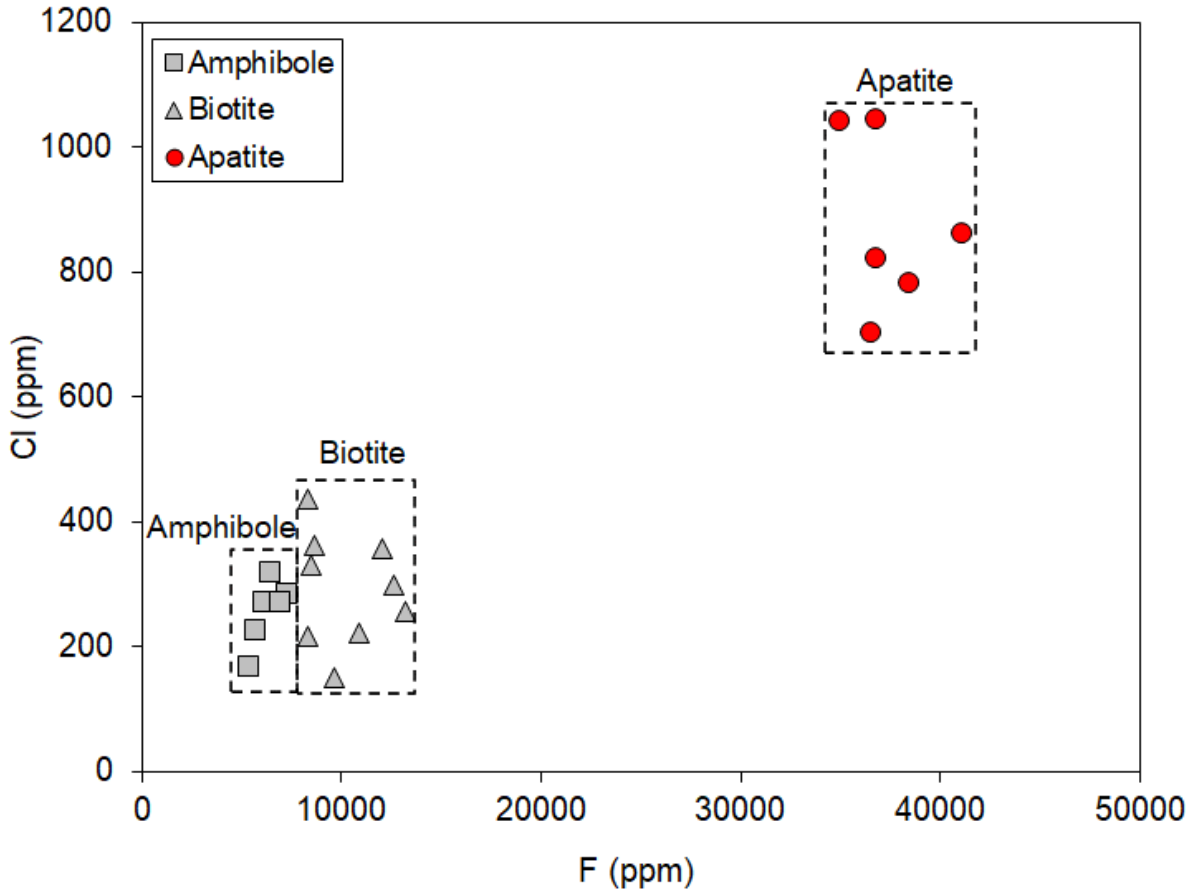

Fig. 13. Variations of F and Cl contents of amphibole, biotite, and apatite from the gabbronorites of the Lac à l'Orignal deposit.

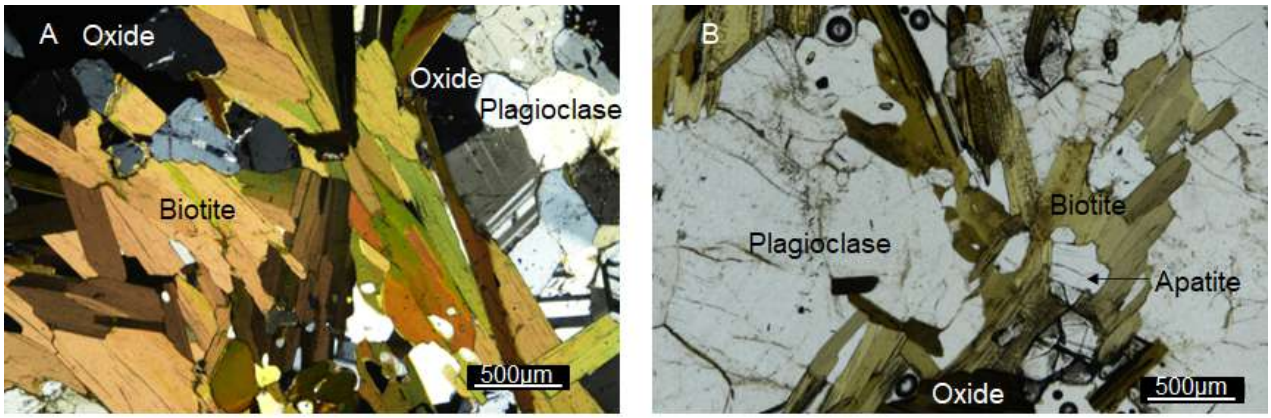

Fig. 14. Textural relationships of amphibole from the Lac à l'Orignal deposit (transmitted light). (A) and (B) Tabular biotite crystals associated with plagioclase and Fe oxide (ilmenite and magnetite) crystals. A and B are taken under cross- and plane-polarized light, respectively.

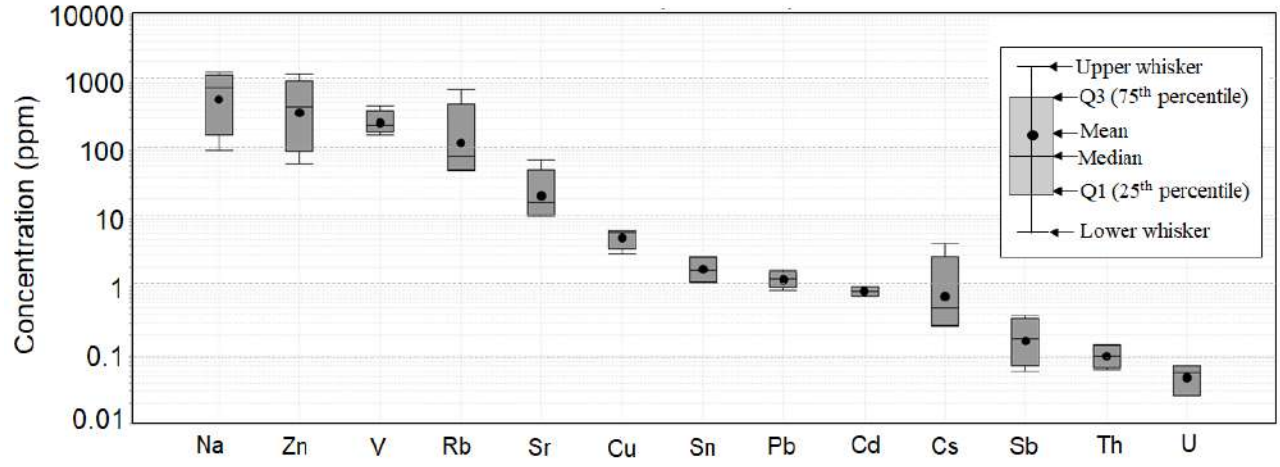

Fig. 15. Concentrations of selected trace elements in biotite.

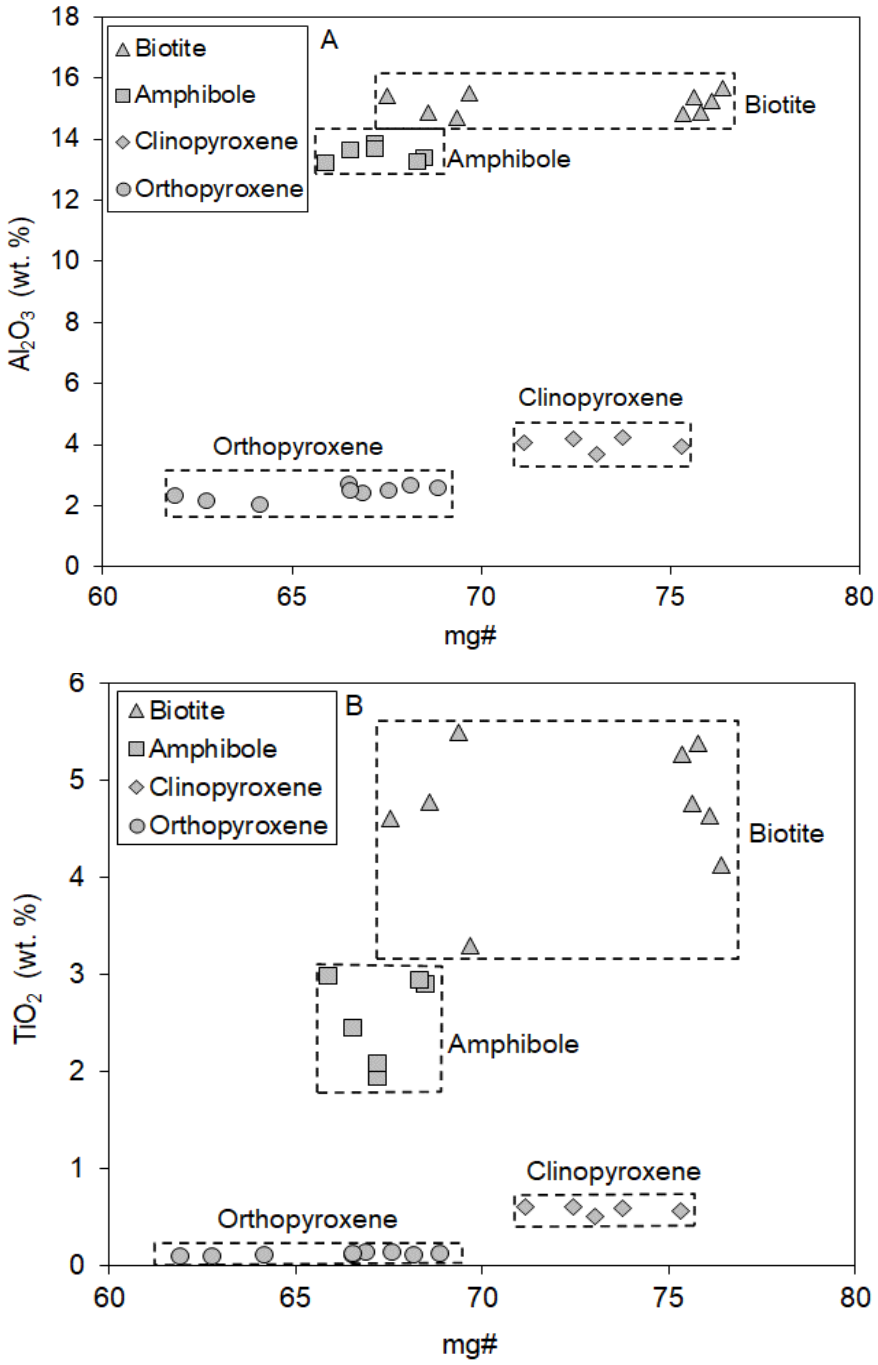

Fig. 16. Relationships between Al_2O_3 and TiO_2 contents with mg numbers (mg# = Mg/(Mg + Fe^{2+})) of orthopyroxene, clinopyroxene, amphibole, and biotite from the gabbronorites of the Lac à l'Orignal deposit. (A) Al_2O_3 contents vs mg# of orthopyroxene, clinopyroxene, amphibole, and biotite; (B) TiO_2 contents vs mg# of orthopyroxene, clinopyroxene, amphibole, and biotite.

Apatite ($Ca_5(PO_4)_3F$): Apatite occurs as individual crystals in melanocratic, magnetite- and ilmenite-rich, layers (Fig. 17A and B), individual crystals associated with plagioclase (Fig. 17C and D) and orthopyroxene (Fig. 17E and F), and inclusions within orthopyroxene (Fig. 8E and F). The highest modal abundances of apatite (> 5%) are associated with the oxide minerals in melanocratic layers. Apatite crystals associated with plagioclase (Fig. 17C and D) and orthopyroxene (Fig. 17E and F) and occurring as inclusions within orthopyroxene (Fig. 8E and F) are euhedral to subhedral. Apatite crystals associated with magnetite and ilmenite within melanocratic layers are subhedral to anhedral (Fig. 17A and B).

Apatite crystals have narrow ranges of CaO (54.7-55.3 wt.%) and P_2O_5 (41.3-41.8 wt.%) concentrations. The SiO_2 (0.07-0.22 wt.%) and MnO (0.02-0.05 wt.%) contents are low (Table 4). F (3.66-4.11 wt.%) concentrations are higher than Cl (0.07-0.1 wt.%) and H_2O (0.02-0.11 wt%; in form of -OH; Table 4). The concentration of the halogens F and Cl are higher than those of amphibole and biotite (Fig. 13). Mole fraction values of fluor-(FAp), chlor-(CAp), and hydroxylapatite (HAp) are calculated following the procedure described by Piccoli and Candela (2002). The ternary plot of FAp-CAp-HAp indicates that the apatite in the Lac à l'Orignal deposit is fluorapatite (Fig. 18).

The F contents of the apatite crystals were measured using EPMA from prismatic cross-sections in thin sections (cross-section cut parallel to the c-axis of the crystal). Measured X-ray flux from apatite is affected by crystal orientation (Stormer et al., 1993, Goldoff et al., 2012, Webster and Piccoli, 2015). Consequently, slight variations in crystal orientation can significantly affect measured F concentrations. Measured Cl contents are less influenced by crystal orientation (Webster and Piccoli, 2015). Pure fluorapatite contains 3.77 wt.% F (Piccoli and Candela, 2002), which suggests measured F contents of 3.77 wt% in the Lac à l'Orignal deposit are overestimates from crystals that were not transected perfectly parallel to their c crystallographic axis (Webster and Piccoli, 2015).

Apatite crystals have a narrow range in their CaO/P_2O_5 ratios (1.31-1.33), but high variability in their F/Cl ratios (33.7-52.3, Fig. 19). Common trace elements include Mg (943 ± 492 ppm), Ti (316 ± 682 ppm), Zn (31 ± 24 ppm) As (6.6 ± 5.4 ppm), Th (7.3 ± 13 ppm), V (3.1 ±1.5 ppm), U (2.8 ± 4 ppm), Cu (4.2 ± 6.5 ppm), Ba (1.2 ± 0.4 ppm), Pb (1.02 ± 0.5 ppm), Cd (1 ± 0.5 ppm), Sn (0.9 ± 0.4 ppm) and Sb (0.15 ± 0.1 ppm). The Sr concentration of apatite (1300 ± 306 ppm) is higher than the concentration of all other trace elements in the crystal structure (< 1000 ppm; Fig. 20).

The concentrations of P, F, and Cl analyzed by LA-ICP-MS were also not reported (Table 5) because these elements cannot be measured reliably using LA-ICP-MS. Concentrations of Si, Sr, Na, and Mn analyzed by EPMA, and LA-ICP-MS are similar (Table 5). Concentrations of As in apatite analyzed by EPMA are higher than those analyzed by LA-ICP-MS (Table 5 and Fig. 21). Ca (36.9-42.6 wt.%), P (18.2-19.6 wt.%), Si (0.1-1.7 wt.%), F (4.1-5.9 wt.%), and Cl (0.2-0.4 wt.%) contents analyzed by SEM have wider ranges than those analyzed by EPMA (Table 5).

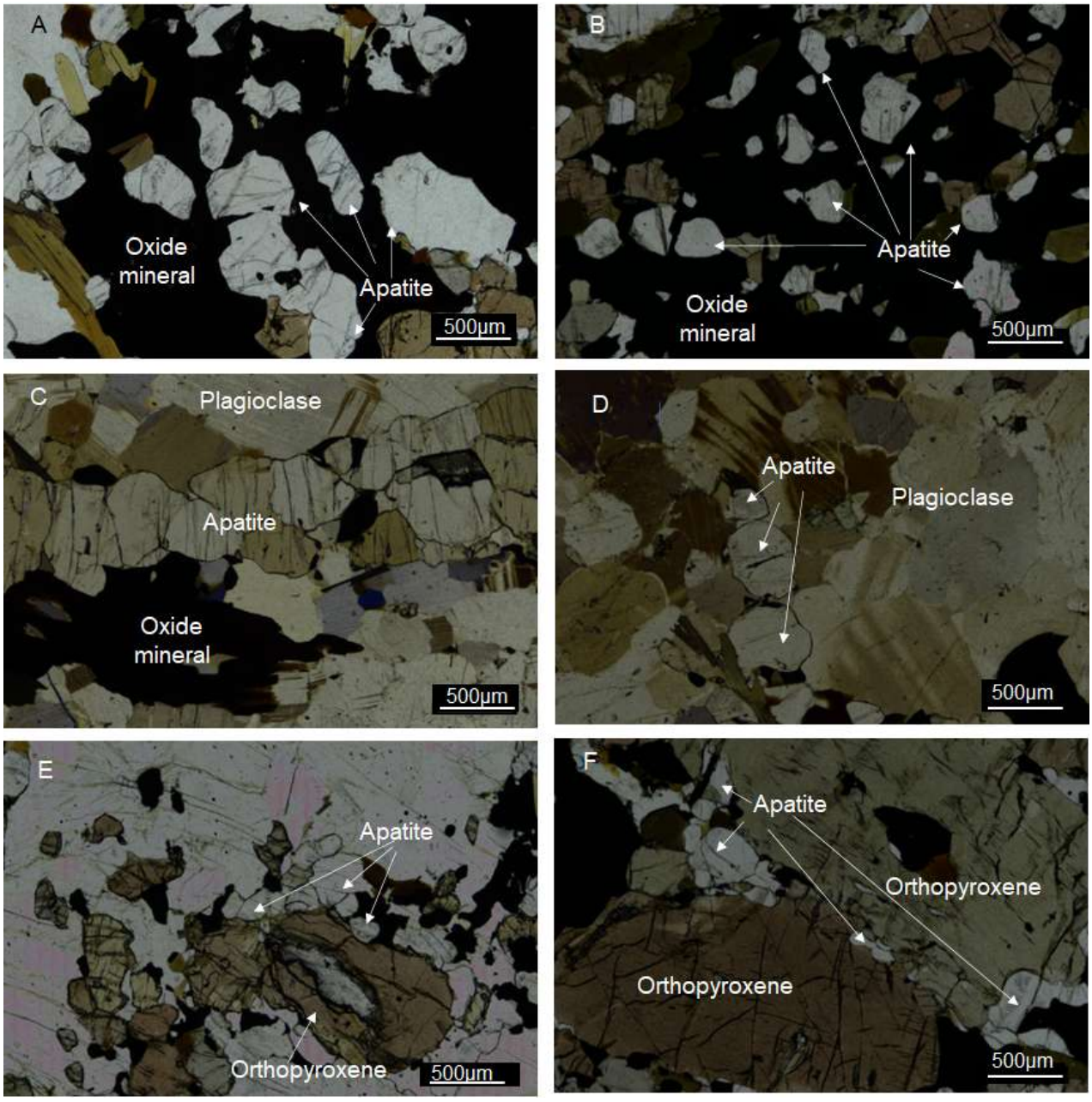

Fig. 17. Textural relationships of apatite and associated minerals from the Lac à l'Orignal deposit (transmitted light). (A) and (B) Apatite crystals of different sizes within a melanocratic, magnetite- and ilmenite-rich layer (plane-polarized light); (C) and (D) Apatite crystals associated with plagioclase (cross-polarized light); (E) and (F) Apatite crystals associated with orthopyroxene (plane-polarized light).

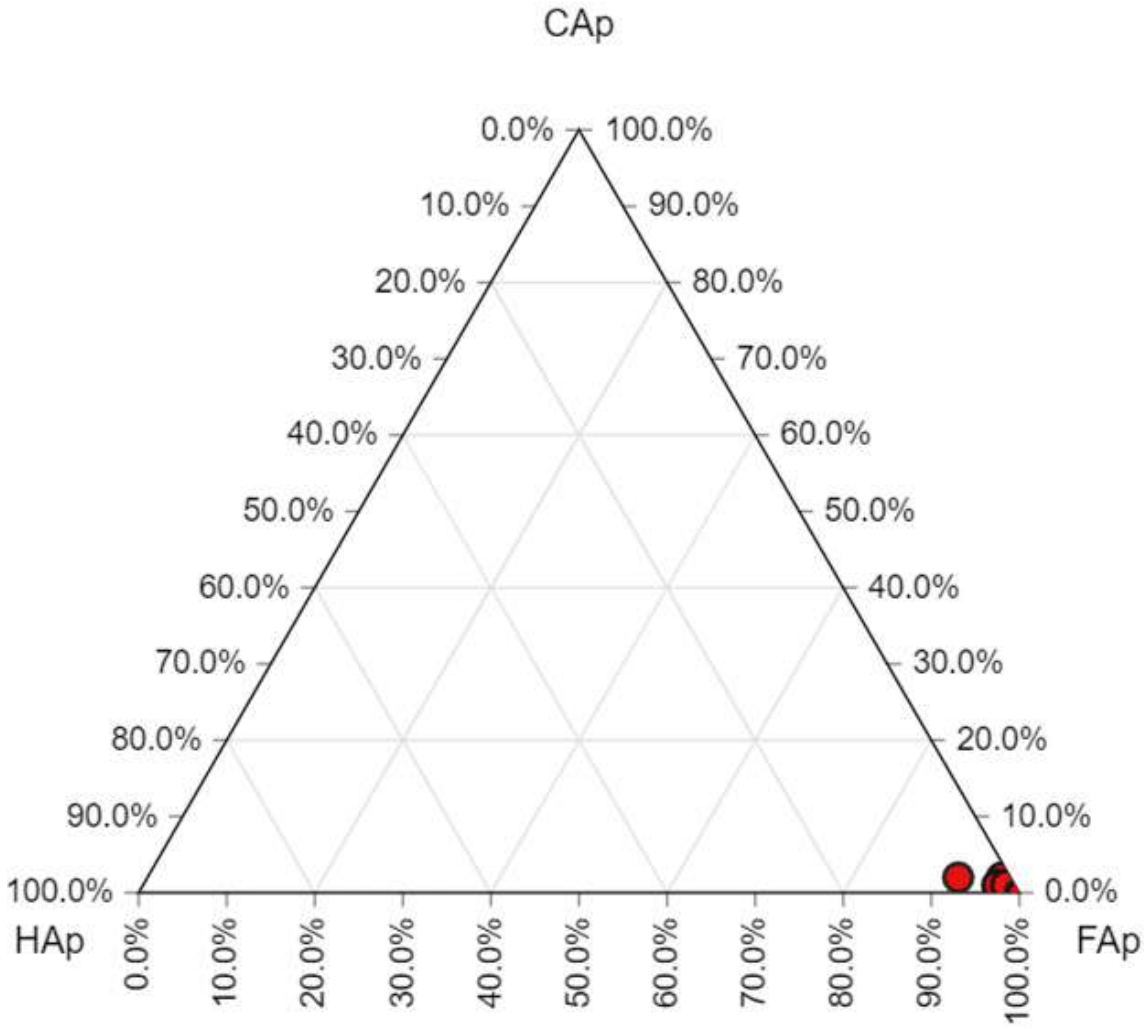

Fig. 18. Ternary plot of fluor- (FAp), chlor-(CAp), and hydroxyl-apatite (HAp) showing variability of F-Cl-OH in the halogen-site of apatite from the Lac à l'Orignal deposit.

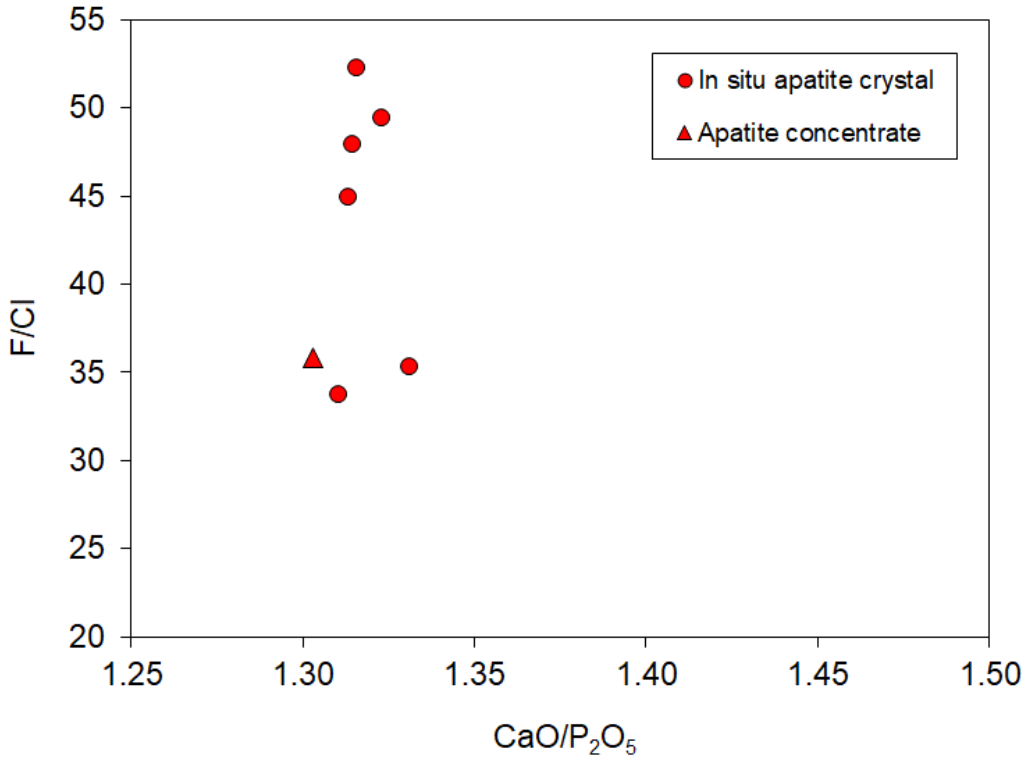

Fig. 19. Variations of F/Cl and CaO/P_2O_5 ratios of *in situ* apatite crystals from the Lac à l'Orignal deposit (EPMA analysis). Triangle is an average value of F/Cl and CaO/P_2O_5 ratios from the apatite concentrate after beneficiation by SGS (apatite concentrate analysis by Actlabs, Prayon, and Nutrien).

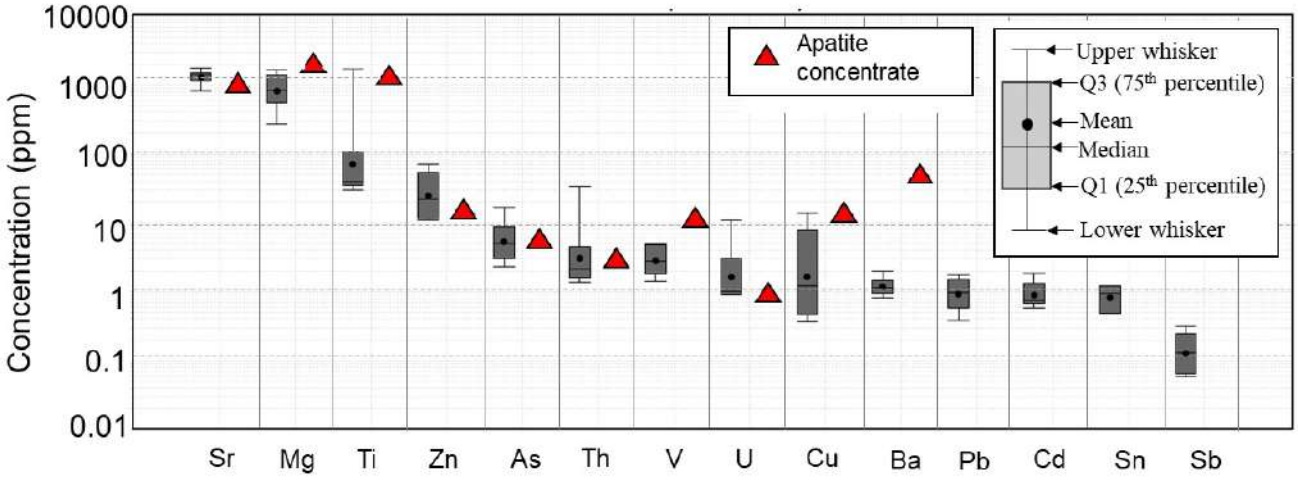

Fig. 20. Concentrations of selected trace elements from *in situ* apatite. Concentrations of trace elements of the apatite concentrate analyzed by Actlabs are also included.

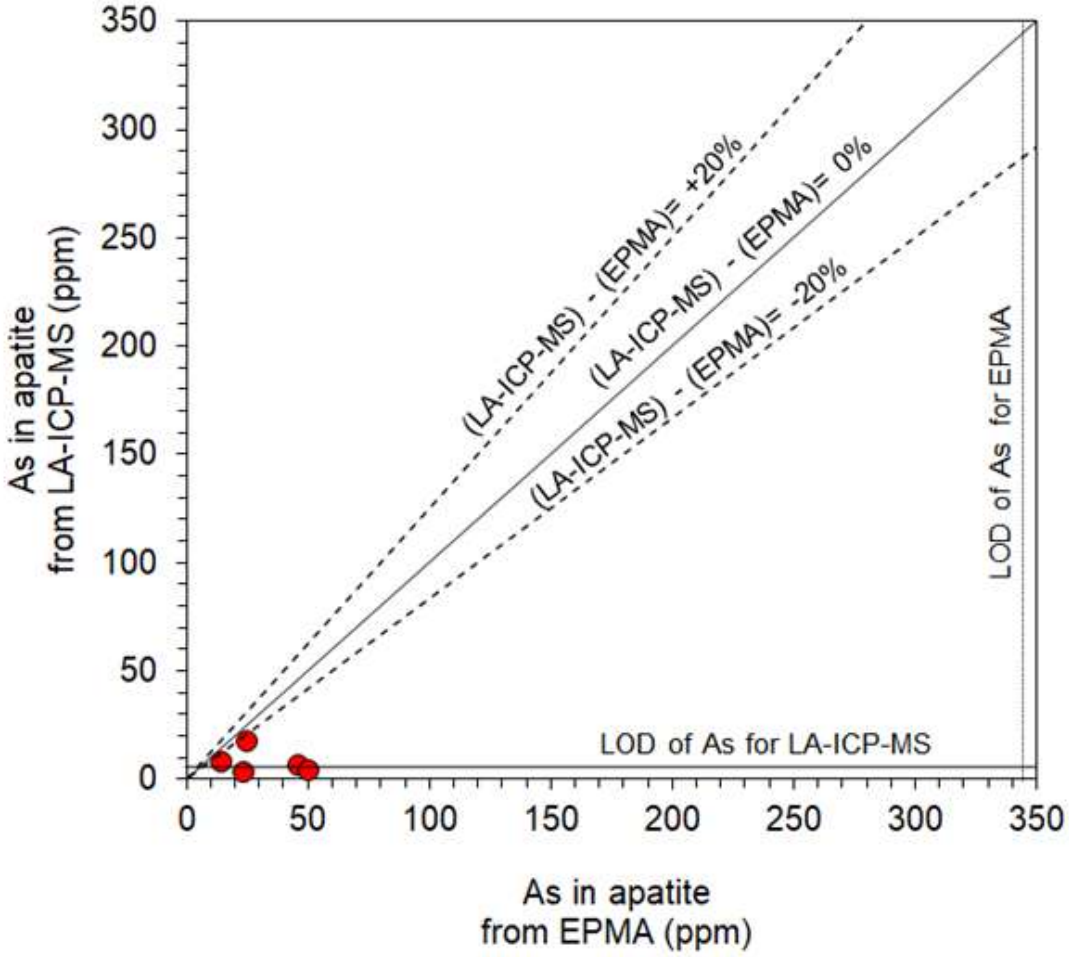

Fig. 21. Comparisons of As contents in apatite analyzed by EPMA and LA-ICP-MS. LOD = lower limit of detection.

Ilmenite ($(Fe,Ti)_2O_3$): Ilmenite is one of the two major oxide minerals forming the melanocratic, oxide-rich layers in the gabbronorite (Fig. 22A and B). Ilmenite crystals are euhedral to subhedral, ranging in size from ~0.2 mm to > 3 mm. Hematite exsolution lamellae are common in individual ilmenite crystals (Fig. 22A). Exsolution lamellae range in width from < 1 μm to > 10 μm. Ilmenite crystals without exsolution lamellae also occur in more magnetite-rich areas of the deposit (Fig. 22B).

Ilmenite crystals with and without hematite exsolution laminae possess a narrow range of TiO_2 (46.2-50.0 wt.%) and FeO (38.4-40.6 wt.%) concentrations. The MnO (0.42-0.84 wt.%), MgO (0.75-1.98 wt.%), and Cr_2O_3 ($Cr_2O_3 \leq 0.01$ wt.%) contents are low (Table 4).

Concentrations of Ti and Fe analyzed by LA-ICP-MS (Fe not reported) and SEM have wider ranges than those analyzed by EPMA (Table 5). Concentrations of Mg and Mn analyzed by LA-ICP-MS, EPMA, and SEM, however, possess similar ranges (Table 5).

Magnetite (Fe_3O_4): Magnetite is the other major oxide phase forming melanocratic, oxide-rich layers (Fig. 23A and B). Magnetite crystals are euhedral to subhedral and range in size from ~0.2 mm to > 3 mm. Al-spinel occurs as external granule exsolution along the crystal boundaries of some magnetite crystals (Fig. 23A). Magnetite is associated with ilmenite and commonly occurs with apatite and orthopyroxene as intercumulate phases in melanocratic layers (Fig. 17A and B). Rarely, magnetite and ilmenite are associated with silicates in these layers (Fig. 17C).

Magnetite crystals also exhibit a narrow range of Fe_2O_3 (67.6-68.1 wt%) and FeO (31.0-31.3 wt%) concentrations. The TiO_2 (0.07-0.25 wt %), MgO (0.03-0.11 wt%), and MnO (≤0.01 wt. %) contents of magnetite are low (Table 4).

Sulfide minerals: Sulfides are accessory minerals (< 3%) in melanocratic, oxide-rich layers. The most common sulfide mineral is pyrrhotite ($Fe_{1-x}S$, X=0 to 0.17; Fig. 24A). Pyrrhotite is commonly replaced by chalcopyrite ($CuFeS_2$; Fig. 24B) and pentlandite ($(Fe,Ni)_9S_8$; Fig. 24C). Sulfide minerals also occur as inclusions within plagioclase (Fig. 25C) and orthopyroxene crystals (Fig. 24D).

8.2. Rare earth elements (REEs) of apatite and silicate minerals

The REEs are trace elements with atomic numbers of 57-71 (La, Ce, Pr, Nd, Pm, Sm, Eu, Gd, Tb, Dy, Ho, Er, Tm, Yb, Lu). Y is also commonly included in this series. Total concentrations of REE in apatite crystals (2940 ± 1100 ppm) are significantly higher than that of plagioclase (20.6 ± 7.7 ppm), orthopyroxene (4.4 ± 2.1 ppm), and biotite (5.1 ± 2.5 ppm) because REEs preferentially partition into apatite (Prowatke and Klemme, 2006; Owens et al., 2019; Ayers and Watson, 1993).

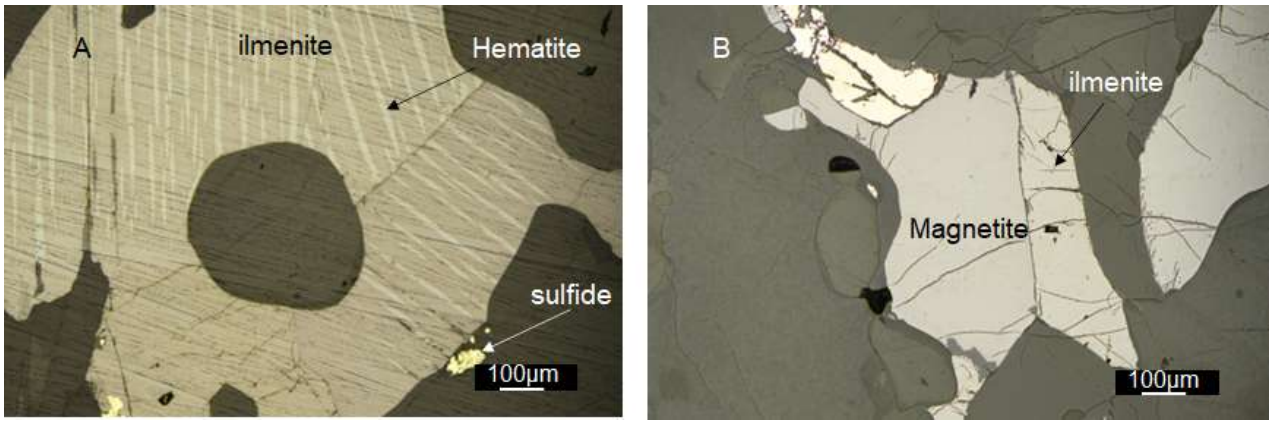

Fig. 22. Textural relationships of ilmenite and associated minerals from the Lac à l'Orignal deposit (reflected light). (A) Hematite exsolution lamellae within ilmenite crystals producing the zebra-striped pattern (plane-polarized light); (B) Ilmenite crystal without hematite exsolution lamellae (plane-polarized light).

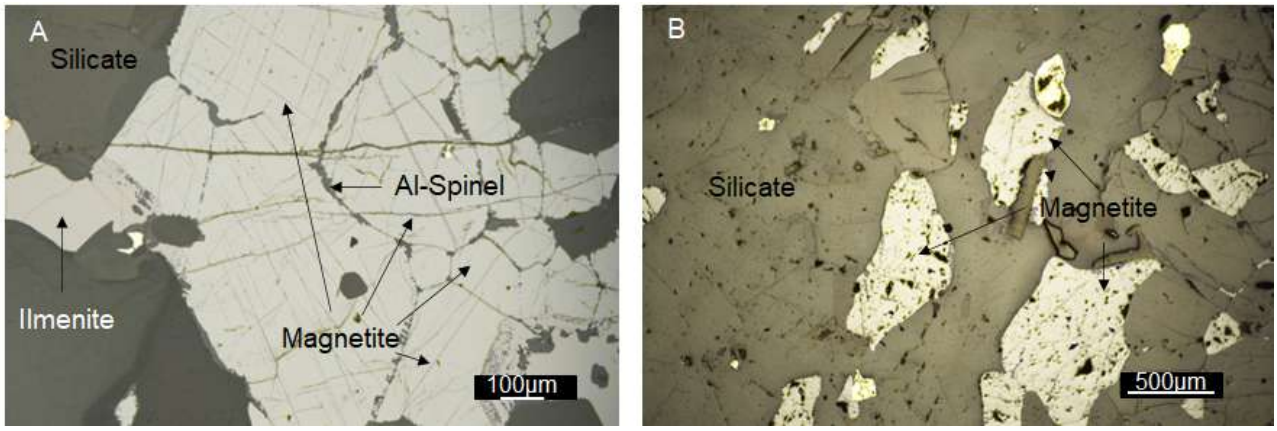

Fig. 23. Textural relationships of magnetite and associated minerals from the Lac à l'Orignal deposit (reflected light). (A) Magnetite crystals associated with external granule exsolution of Al-spinel (plane-polarized light); (B) Magnetite crystals associated with silicate minerals (plane-polarized light).

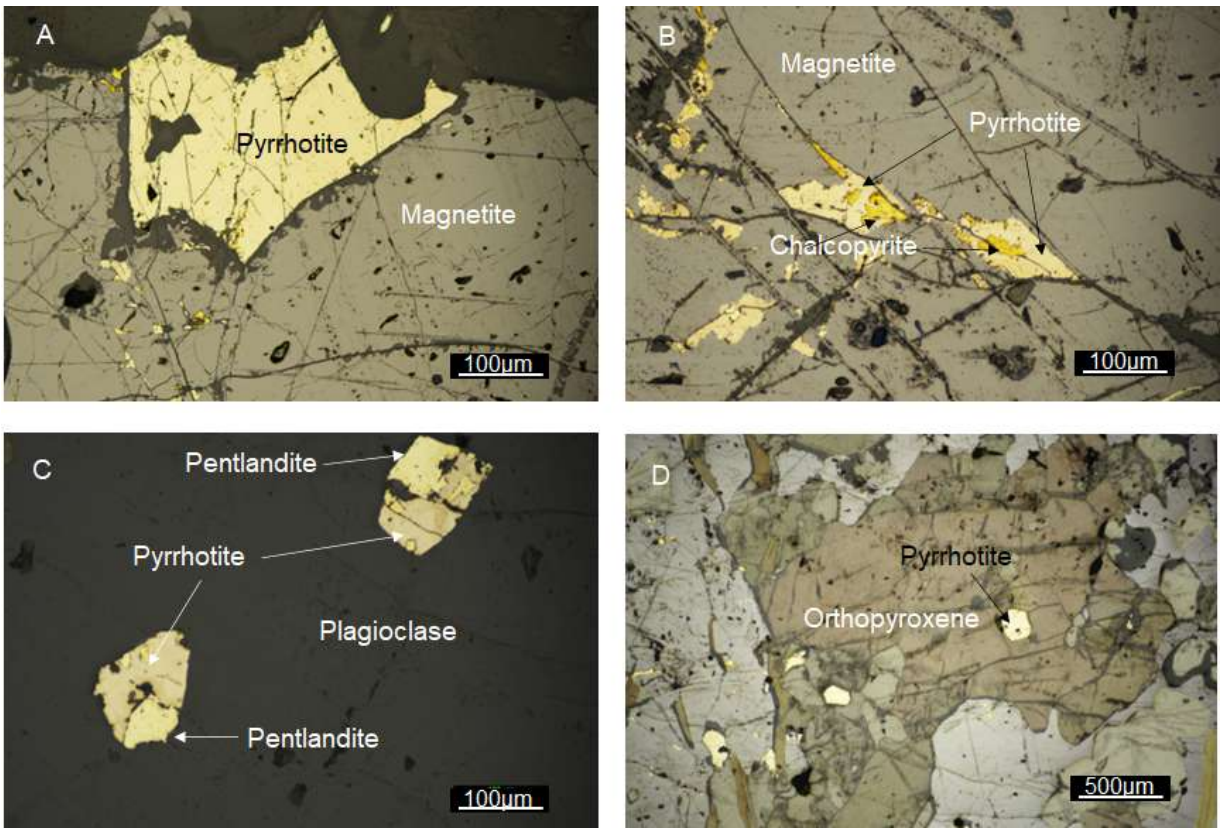

Fig. 24. Textural relationships of ilmenite and associated minerals from the Lac à l'Orignal deposit. (A) Pyrrhotite crystal associated with magnetite (plane-polarized reflected light); (B) Pyrrhotite and chalcopyrite crystals associated with magnetite (plane-polarized reflected light); (C) Pentlandite and pyrrhotite crystals within plagioclase (plane-polarized reflected light); (D) Pyrrhotite inclusion within orthopyroxene crystal (plane-polarized transmitted and reflected light).

Concentrations of REEs are conventionally represented as normalized (ratios) values with respect to a standard. Values are characteristically normalized with respect to a chondrite, which is a type of meteorite (Fig. 25A-C; Pourmand et al., 2012). Chondrite-normalized REE patterns of plagioclase (Fig. 25A), orthopyroxene (Fig. 25B), and apatite (Fig. 25C) reveal three distinct trends, which are a) total REE concentrations are the highest in apatite followed by plagioclase, and orthopyroxene, b) both apatite and plagioclase have higher concentrations of light rare earth elements (LREE include La, Ce, Pr, Nd, Sm, Eu, Gd) than heavy rare earth elements (HREE include Tb, Dy, Ho, Er, Tm, Yb, Lu), and c) plagioclase and apatite show prominent positive and negative Eu anomalies, respectively. Positive and negative Eu anomalies are defined by chondrite-normalized Eu concentrations that are higher and lower than those of its neighboring Sm and Gd concentrations (Rollinson, 2014).

8.3. Chemistry of Lac à l'Orignal apatite concentrate

Beneficiation produces an apatite concentrate that has similar CaO (50.7-54.7 wt. %) and P_2O_5 (40.5-41.2 wt.%) contents to *in situ* apatite crystals (CaO= 54.9 ±0.42 wt.%, P_2O_5= 41.7±0.26 wt.%; Table 6). CaO/P_2O_5 (1.25-1.33) and F/Cl (34.1-37.5) ratios of the concentrate and *in situ* crystals are also similar (Table 6 and Fig. 19).

The F contents of the apatite concentrate analyzed by Actlabs (3.0 wt.%), Prayon (2.98 wt.%), and Nutrien (3.12 wt.%) are lower than those analyzed from *in situ* apatite crystals using EPMA (3.1-4.47 wt.%) and SEM (3.7-5.9 wt.%; Table 6). This slight overestimation from *in situ* apatites is a consequence of the previously explained issues of analyzing imperfectly oriented crystals. The Cl content of the concentrate analyzed by Actlabs (800 ppm) and Prayon (873 ppm) are similar to the Cl contents analyzed from *in-situ* apatite crystals using EPMA (837±132 ppm) because crystallographic orientation has little effect on the ability of EPMA to analyze Cl (Table 6). The analysis of Cl concentrations of *in situ* apatite crystals using TIMA X-ray (2000-3000 ppm) and SEM (2000-4000 ppm) are significantly higher than those of the apatite concentrate (Table 6).

The minor element ratio (MER) of the apatite concentrate is low (0.02-0.03, Table 7). A comparison of concentrations of selected minor or trace elements (Si, Fe, Al, Mg, Ti, Na, Sr, As, Cd, Th, U, and Pb), which generally occur as impurities within apatite, is provided in Table 8. Concentrations of selected trace elements from the concentrate are similar to those of *in situ* apatite crystals (Fig. 20). Total concentrations of REEs in the apatite concentrate (2110 ppm) is lower than the average (total) concentration of REE (2940 ± 1100 ppm) of *in situ* apatite crystals (Table 6). However, the chondrite-normalized REE patterns of *in situ* apatite crystals and the apatite concentrate show that the concentrations of REEs of the apatite concentrate are generally within the ranges of concentrations of REEs of *in situ* apatite crystals (Fig. 25C).

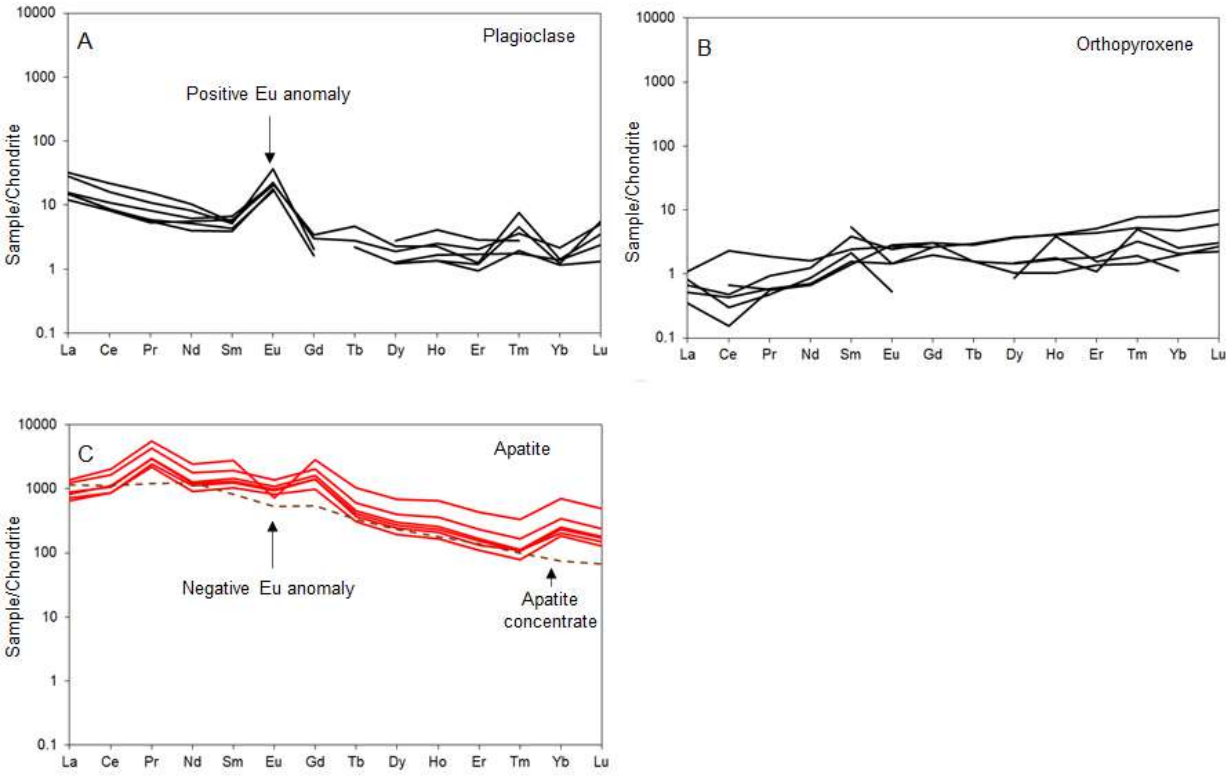

Fig. 25. Chondrite-normalized REE patterns of plagioclase, orthopyroxene, and *in situ* apatite crystals from the Lac à l'Orignal deposit. Chondrite-normalized REE pattern of the apatite concentrate after metallurgical processing (analyzed by Actlabs) is included as a dashed line.

Table 6. Comparisons by various analytical techniques of CaO, P_2O_5, F, Cl, CaO/P_2O_5, F/Cl, and REE contents of *in situ* apatite crystals and concentrate produced by metallurgical processing.

Laboratory/ Instrument	No of crystal	CaO (wt%)	P_2O_5 (wt%)	CaO/P_2O_5	F (wt%)	F (ppm)	Cl (wt%)	Cl (ppm)	F/Cl	REE (ppm)
***In situ* apatite crystal**										
Analyzed by SGS (*by TIMA X-Ray*)	4		42.0 ±3.55				0.2-0.3	2000-3000		
Analyzed by SGS (*by SEM*)	26				3.7-5.9	37000-59000	0.2-0.4	2000-4000	29.5*	
Analyzed by Queen's University (*CaO, P_2O_5, F, and Cl are analyzed by EPMA and REE is analyzed by LA-ICP-MS*)	n=19 (for CaO, P_2O_5, F, and Cl); n=24 (for REE)	54.9 ±0.42	41.7 ±0.26	1.32	3.1-4.47 (avg. 3.73±0.36)	31000-44700	0.0671-0.118	671-1180 (avg 837±132)	33.7-52.3**	2940 ± 1100
Apatite concentrate recovered after beneficiation										
Analyzed by Actlabs (*CaO, P_2O_5, and REE are analyzed by ICP-MS, Cl and F are analyzed by instrumental neutron activation, and fusion with ion selective electrode, respectively*)		54.7	41.2	1.33	3.0	30000	0.08	800	37.5	2110
Analyzed by Prayon		53.9	40.5	1.33	2.98	29800	0.09	873	34.1	
Analyzed by Nutrien		50.7	40.5	1.25	3.12	31200				

* Based on 1 measurement where both F and Cl concentrations were analyzed.
** From Table 4

Table 7. Comparison of calculated MER of the apatite concentrate from three laboratories. Concentrations of Fe_2O_3, Al_2O_3, MgO, and P_2O_5 are also included.

	Actlabs	Prayon	Nutrien
	(wt.%)		
Fe_2O_3	0.73	0.73	0.42
Al_2O_3	0.25	0.25	0.23
MgO	0.3	0.3	0.22
P_2O_5	41.2	40.4	40.5
MER*	0.03	0.03	0.02
*MER= $(Fe_2O_3+Al_2O_3+MgO)/P_2O_5$			

Table 8. Comparisons from three laboratories of compositional data of selected elements from the apatite concentrate produced by metallurgical processing at SGS.

	Actlabs	Prayon	Nutrien
	(ppm)		
Si*	4340	4760	n.a
Fe*	5104	5131	2937
Al*	1323	1297	1218
Mg*	1800	1821	1320
Ti*	1271	1240	232
Na*	519	555	816
Sr	961	950	943
As	5.0	0.432	n.a
Cd	0.49	2.13	<1
Th	2.66	<5	n.a
U	0.85	<0.85	n.a
Pb	1.0	<20	<1
n.a: not analyzed * Recalculated from their oxide concentrations.			

9. Discussion

9.1. Variability of concentration data and analytical techniques

Understanding analytical techniques are important to assess the quality (precision and accuracy), of elemental concentration data of minerals. Some analytical techniques are easy to apply and provide rapid data of reasonable quality. Conversely, other analytical techniques are labor-intensive but provide data with a much higher degree of precision and accuracy. For pilot or preliminary studies such as presented herein, rapid and easier analytical methods can provide the broad brushstrokes required for an initial assessment. However, detailed investigations that aim to understand the fine details of ore deposits require higher-quality data using more labor-intensive analytical techniques. Thus, the analytical methods used, and the type of data generated often become more complex and laborious as projects develop.

Elemental concentrations of both ore (apatite) and gangue minerals (plagioclase, orthopyroxene, clinopyroxene, and biotite) are analyzed *in situ* using EPMA, LA-ICP-MS, and SEM. Data produced using an SEM are less time-consuming to obtain than data generated using EPMA and LA-ICP-MS. Consequently, SEM-generated compositional data possess wider ranges in values than data produced by EPMA, and LA-ICP-MS. EPMA and LA-ICP-MS provide data with better accuracy and precision. Therefore, SEM-generated data produces the broad brushstrokes required for the rapid characterization of rocks, but these data are generally not suitable for answering more complex, targeted questions as projects evolve. Other more time-consuming and labor-intensive methods such as EMPA and LA-ICP-MS are required.

The EPMA is very reliable for analyzing concentrations of major elements and some trace elements that have concentrations no lower than 100-500 ppm, which is the lower limit of detection (LOD). Most major and trace elements whose concentrations are > 500 ppm analyzed by EPMA, and LA-ICP-MS are approximately similar (Table 5, Fig. 7, and Fig. 10). However, LA-ICP-MS produces elemental data at even lower concentrations well below 100 ppm. Depending on the element, this technique has a LOD of between 1 and 20 ppm. For example, EPMA overestimated As concentrations of *in situ* apatites (15-51 ppm). Analysis by LA-ICP-MS of *in situ* apatites yielded much lower concentrations (2-17 ppm, Table 5 and Fig. 21), as did whole rock analysis using ICP-MS at Actlabs (< 10 ppm; Fig. 20). The overestimation of As by EPMA is related to the higher LOD for this element when analyzed by EPMA (Fig. 21). Therefore, understanding the limits of various analytical methods, such as LOD, is critical for properly interpreting and framing the significance of compositional data.

Some elements, such as F, Cl, and P, cannot be measured reliably using LA-ICP-MS because these elements are difficult to ionize. EPMA is the only suitable method for analyzing concentrations of these elements. Furthermore, Cl concentrations of *in situ* apatite crystals analyzed by TIMA X-ray (2000-3000 ppm) and SEM (2000-4000 ppm; Table 6) are higher than those of *in situ* apatite crystals analyzed by EPMA (837±132 ppm), and the apatite concentrate analyzed by Actlabs (800 ppm using instrumental neutron activation method) and Prayon (873 ppm), suggesting that TIMA X-ray and SEM overestimate the Cl concentrations of apatite. Similarly, F concentrations of *in situ* apatite crystals analyzed by SEM (3.7-5.9 wt.%) also overestimate that of apatite crystals because pure fluorapatite contains only 3.77 wt.% of F.

Therefore, analysis of halogen concentrations using TIMA X-ray and SEM do not provide data with high accuracy and precision.

It is important to note that EMPA is also the best technique for analyzing minerals with extensive exsolution lamellae, such as the ilmenite in the Lac à l'Orignal deposit. Ti contents analyzed by LA-ICP-MS possess wider ranges than those analyzed by EPMA (Table 5) because the wider beam diameter of LA-ICP-MS (35µm) than that of EPMA (5–10µm) interrogates a higher degree of elemental heterogeneity within ilmenite. An advantage of analysis by LA-ICP-MS is that more elements can be analyzed more quickly in a single run than using EPMA.

Total concentrations of REE of *in situ* apatite crystals using LA-ICP-MS (2936 ± 1108 ppm) are higher than that of the apatite concentrate analyzed by ICP-MS (2105 ppm; Table 6). The ICP-MS method analyzes elemental concentrations from solutions in which minerals are dissolved. Higher values in the concentrate likely reflect the weighted average of apatite crystals present in the gabbronorite composing the Lac à l'Orignal deposit. Therefore, the total concentration of REE (Table 6) and chondrite normalized REE pattern of the apatite concentrate (Fig. 26C) are slightly different from those of *in situ* apatite crystals.

In summary, it is important that compositional data from minerals are interpreted with an understanding of the analytical techniques used to obtain these data. Such an appreciation will assist with identifying anomalies that are useful for exploration or simply artifacts produced by the various analytical methods employed.

9.2. Significance of apatite halogen (F and Cl) content

The F and Cl are ubiquitous trace elements in apatite and are corrosive to equipment for the production of phosphoric acid from apatite concentrate (Chandra et al., 2017; Schorr and Valdez, 2017). Therefore, understanding the distributions of these halogens is critical for discriminating high-grade phosphate ore zones with the lowest concentrations of these elements.

Apatite from the Lac à l'Orignal deposit is a fluorapatite (Fig. 18), which is an apatite that contains a significant amount of F. The apatite concentrate from ore zones contains 2.98-3.12 wt. % of F (Table 6), which is lower than the threshold concentration of concern (<3.5 wt.%) for producing phosphoric acid (Table 9, provided by Prayon). F concentrations are lower than that of phosphate rocks used for producing phosphoric acid in Florida-USA (3.6 wt.%), Oron-Israel (3.8 wt.%), Safi-Morocco (4.1 wt.%; Schorr et al., 2010). Considering the global demand for F (Schulz et al., 2017; Will, 2016), the removal of F during phosphoric acid production could produce a saleable by-product (Peng et al., 2022).

The Cl contents of *in situ* apatite crystals (837± 132 ppm) and the concentrate (800-873 ppm; Table 6) are marginally higher than the threshold concentration of Cl (< 600 ppm; Table 9 provided by Prayon) preferred for phosphoric acid production. These Cl concentrations are higher than that of sedimentary phosphate rocks in Florida-USA (500 ppm), Oron-Israel (300 ppm), Safi-Morocco (200 ppm; Schorr et al., 2010). Because Cl cannot be extracted prior to the production of phosphoric acid, dilution of high Cl ore with a concentrate containing apatite with lower Cl contents should produce mixed averages below the concentration threshold required to minimize corrosion of equipment. Advanced methods for the reduction of Cl should also be explored.

Table 9. Threshold concentrations in an ideal phosphate concentrate for producing phosphoric acid (provided by Prayon, 2022).

P_2O_5	36-39 wt.%
CaO	48-52 wt.%
CaO/P_2O_5	<1.5
F	<3.5 wt.%
Cl	<600 ppm
MER	<4.5
Si*	2.33 wt.%
Fe*	<0.49 wt.%
Al*	<0.37 wt.%
Mg*	<0.12 wt.%
Ti	<2600 ppm
Na*	< 0.56 wt.%
As	<5 ppm
Cd	<3 ppm
Th	<22 ppm
U*	<7 ppm
* Recalculated from their oxide concentrations	

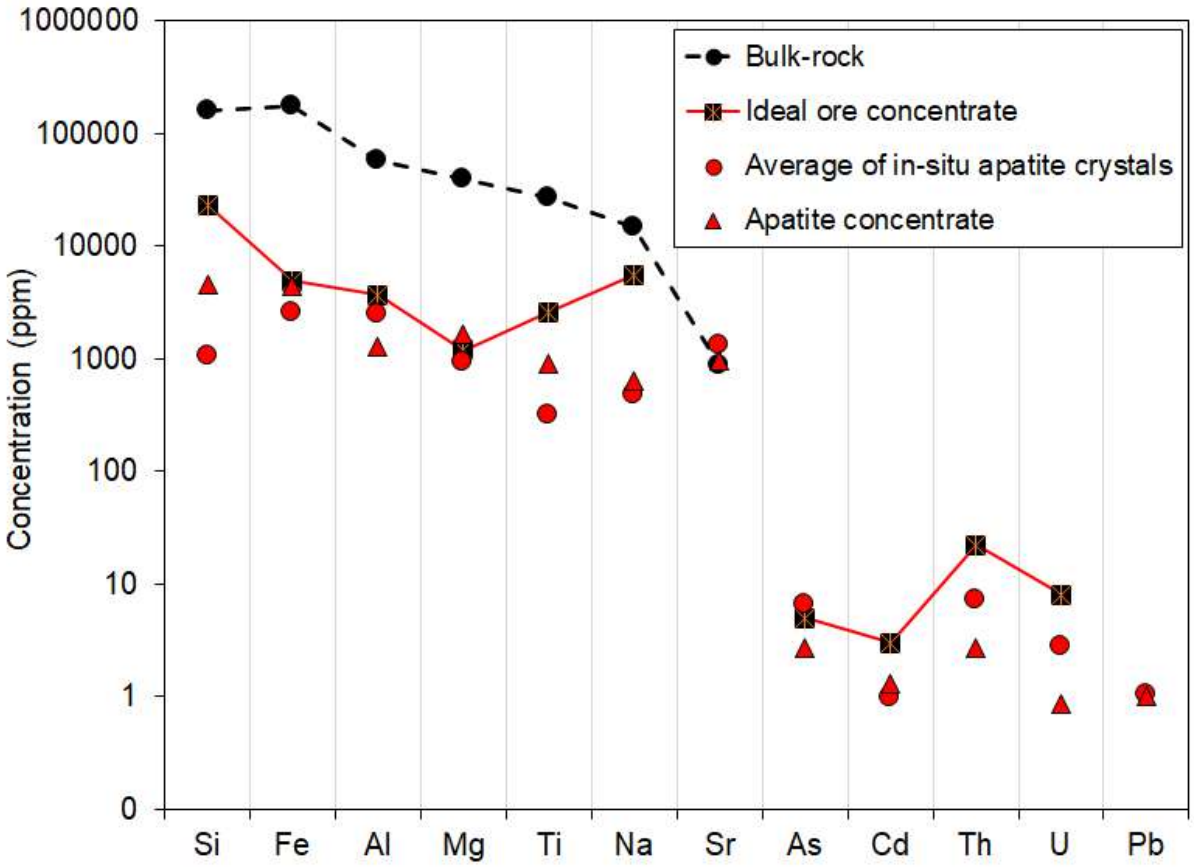

Fig. 26. Comparisons of selected elemental concentrations from whole-rock analysis (AGAT Laboratories), ideal ore concentrate for phosphoric acid production (provided by Prayon), average of *in-situ* apatite crystals (Queen's University), and apatite concentrate (average of Actlabs, Prayon, and Nutrien).

9.3. Apatite of the Lac à l'Orignal deposit as an ESG-compliant source of P

The apatite concentrate must satisfy certain chemical assay criteria for producing phosphoric acid (Table 9). In the Lac à l'Orignal deposit, P_2O_5 (40.45-41.95 wt.%) and CaO (50.68-54.87 wt.%) concentrations of *in situ* apatite crystals and the apatite concentrate (CaO= 48-52 wt.%, P_2O_5 = 36-39 wt.%; Table 6), and CaO/P_2O_5 ratios (1.25-1.33; Table 6) are better than required (Table 9). Halogen concentrations are variable with F below concentrations that are deemed too high, whereas Cl contents are slightly higher than ideal values. All other trace element concentrations are below deleterious threshold concentrations (Fig. 26). Such low concentrations of these elements, which include U and Th (Fig. 26), yield an apatite concentrate that when converted to phosphoric acid generates phosphogypsum that may potentially be recycled into plaster and wallboard. In addition, the low abundances of sulfide gangue minerals suggest that the environmental impacts of acid mine drainage from tailings would be minimal. Thus, enriched concentrations of high-quality apatite, low contents of deleterious trace metals, and low abundances of sulfide gangue minerals make the Lac à l'Orignal deposit an attractive ESG-compliant source of North American P for the LFP battery industry.

9.4. Ilmenite and magnetite as secondary commodities

Gabbronorite containing apatite-oxide are relatively new exploration target for phosphate, Ti, and potentially Fe. The anorthosites of the LSJA Complex in the Grenville Province contain Ti in hemo-ilmenite within andesine anorthosite and titanomagnetite within labradorite anorthosite (Charlier et al., 2015 and references therein). Labradorite anorthosite is generally devoid of apatite, whereas andesine anorthosite contains apatite (Hébert et al., 2005). Results reported herein confirm this notion. Ilmenite in melanocratic, oxide-rich layers in the Lac à l'Orignal deposit is hemo-ilmenite (ilmenite with hematite exsolution lamellae) with low contents of Mg (MgO of 0.75-1.98 wt%; Table 4) and Cr (Cr_2O_3 of $\leq$ 0.01 wt.%; Table 4). During beneficiation, elevated Mg in ilmenite decreases the reduction rate of ilmenite to form TiO_2 (Kim, 2015) and high Cr contents decrease the whiteness of TiO_2 pigments for paints (Bonsack, 1970). In the Lac à l'Orignal deposit, a recovery of 46-50 wt.% TiO_2 should be possible from ilmenite (Table 4).

Magnetite could also be an important secondary commodity as a source of Fe. It is concentrated as a by-product of the metallurgical processing of phosphatic ore from the Lac à l'Orignal deposit. In addition to the steel industry, magnetite nanoparticles can be used for magnetic resonance imaging, manufacturing of catalysts, synthesizing of pigment, and magnetic storage (Darezereshki et al., 2018).

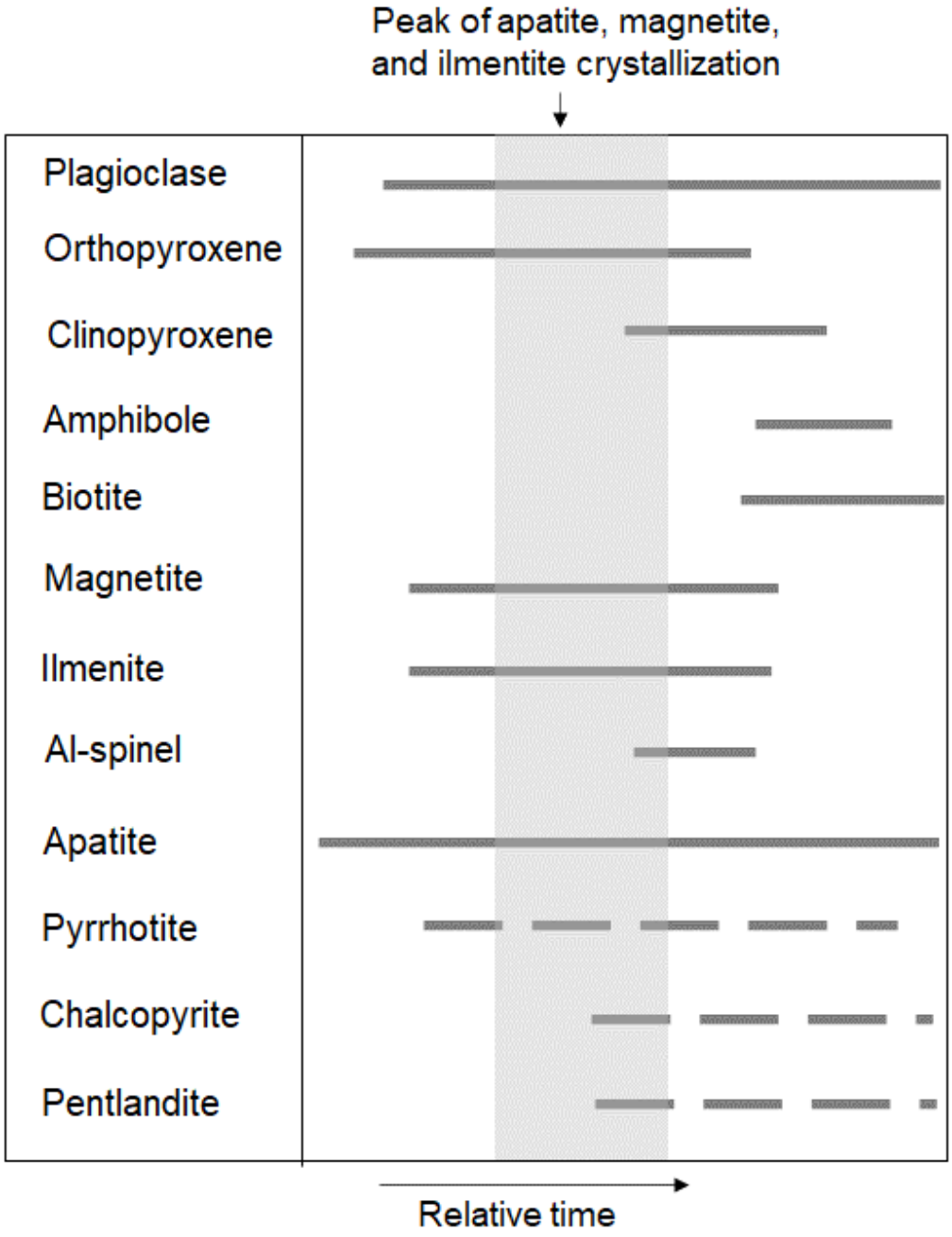

Fig. 27. Paragenesis of minerals composing gabbronorite and anorthosite from the Lac à l'Orignal deposit.

9.5. Mineral paragenesis and timing of apatite crystallization

Mineral paragenesis describes the sequence or timing of mineral formation in any rock. Therefore, understanding mineral paragenesis is critical for properly characterizing an ore deposit and tuning exploration strategies. The petrography and mineral chemistry presented herein are the foundation to deciphering the timing (Fig. 27) and nature of the processes that produced apatite and secondary ore minerals such as ilmenite in the Lac à l'Orignal deposit.

Poikilitic orthopyroxene crystals that envelope plagioclase crystals (Fig. 8A) and plagioclase that contains small inclusions of orthopyroxene (Fig. 5B) suggest that orthopyroxene started to crystallize earlier than plagioclase (Fig. 27). Orthopyroxene and plagioclase continued to crystallize with plagioclase forming to the end of magma crystallization, which produced the gabbronorite of the Lac à l'Orignal deposit.

Apatite inclusions in orthopyroxene (Fig. 8E and F) and plagioclase (Fig. 5B), and the close association of apatite with these same minerals (17C-F), suggest that apatite formed before orthopyroxene and plagioclase and continued to crystallize with these minerals (Fig. 27). The concentration of apatite with magnetite and ilmenite in melanocratic layers (Fig. 17A and B) implies that the major phase of apatite crystallization occurred simultaneously with the crystallization of magnetite and ilmenite (Fig. 28). Textural relationships within melanocratic layers (Fig. 12A and B) further suggest that orthopyroxene started to form before magnetite and ilmenite (Fig. 27). The presence of Al-spinel along the crystal boundaries of magnetite (Fig. 23A) suggests that Al-spinel formed after magnetite through granule exsolution from magnetite (Fig. 27).

The association of clinopyroxene with orthopyroxene (Fig. 11A) suggests simultaneous crystallization from the magma. The conversion of orthopyroxene to amphibole (Fig. 12B) implies that amphibole crystallized after orthopyroxene. In general, Al_2O_3 and TiO_2 contents of a mafic magma increase as magmatic differentiation progresses (e.g., Tornare et al., 2016). Therefore, progressively increasing concentrations of Al_2O_3 and TiO_2 from orthopyroxene to clinopyroxene, amphibole, and biotite (Fig. 16A and B) suggest that crystallization of orthopyroxene was followed by clinopyroxene, amphibole, and biotite (Fig. 27). These results suggest that the Lac à l'Orignal deposit formed through fractional crystallization by the sequential removal of minerals from the magma.

The negative Eu anomalies in apatite (Fig. 25C) indicate that Eu preferentially partitioned into plagioclase during magma crystallization (e.g., Rollinson, 2014). This process produced plagioclase with positive Eu-anomalies (Fig. 25A). These sympathetic Eu anomalies suggest that apatite and plagioclase crystallized concurrently.

The association of the sulfide minerals, pyrrhotite, chalcopyrite, and pentlandite with oxide minerals (Fig. 24A and B), plagioclase (Fig. 24C), and orthopyroxene (Fig. 24D) records a protracted paragenetic history and intermittent precipitation during magma crystallization (Fig. 28). Replacement of pyrrhotite by chalcopyrite (Fig. 24B) and pentlandite (Fig. 24C) suggest that pyrrhotite crystallized first, followed by chalcopyrite and pentlandite (Fig. 27).

In summary, apatite occurs in both the plagioclase-rich leucocratic layers and oxide-rich melanocratic layers. However, the oxide-rich melanocratic layers contain a significant amount of apatite suggesting that the major phase of apatite crystallization was accompanied by the crystallization of magnetite and ilmenite.

10. Conclusions

1. The host-rock of First Phosphate's Lac à l'Orignal deposit is a gabbronorite composed of plagioclase, orthopyroxene, clinopyroxene, biotite, fluorapatite, ilmenite, and magnetite. Fluorapatite is the primary ore mineral and ilmenite, and magnetite are potentially important secondary commodities.

2. The P_2O_5 concentration of apatite using *in situ* analytical methods is 41.7 ±0.26 wt.%, which is just slightly higher than values (40.5-41.2 wt.%) obtained by whole-rock analyses of the apatite concentrate produced by SGS.

3. The Lac à l'Orignal deposit is a potentially viable source of P for the LFP battery market. P_2O_5 and CaO concentrations and CaO/P_2O_5 ratios are better than required for phosphoric acid production. Halogen concentrations are variable with F below concerning levels, whereas Cl contents are slightly higher than ideal values. Cl concentrations could be managed by mixing ores with different Cl contents. Advanced methods for the reduction of Cl should also be explored.

4. Other elements, such as Si, Fe, Al, Mg, As, Cd, U, and Th of the apatite concentrate are below deleterious threshold concentrations. During phosphoric acid production from beneficiated apatite concentrate, these low trace element concentrations may produce phosphogypsum that could potentially be recycled into plaster and wallboard.

5. The low abundance of sulfide gangue minerals suggests that the environmental risks of acid mine drainage from tailings would be minimal. Such low concentrations of deleterious trace elements and sulfide minerals make the Lac à l'Orignal deposit an attractive ESG-compliant source of North American P for the LFP battery industry.

6. Paragenetic relationships indicate that apatite precipitated throughout the crystallization history of the magma. However, the highest quality phosphatic ore is interpreted to have formed as apatite-magnetite-ilmenite cumulate layers that precipitated early to mid-way through the fractional crystallization process.

7. Further research should focus on the detailed characterization of other First Phosphate properties. The complexity of the LSJA Complex necessitates a comprehensive understanding of the mineralogy and geochemistry of these areas as a counterpoint to the Lac à l'Orignal region. Such a comparison will provide important new information required to fully assess the distribution of high-grade ore zones.

11. References

Ahsan, Z., Ding, B., Cai, Z., Wen, C., Yang, W., Ma, Y., Zhang, S., Song, G., and Javed, M.S. (2021). Recent progress in capacity enhancement of LiFePO4 cathode for Li-ion batteries. Journal of Electrochemical Energy Conversion and Storage, 18(1), 010801.

Alves, P.R. (2008). The carbonatite-hosted apatite deposit of Jacupiranga, SE Brazil: styles of mineralization, ore characterization and association with mineral processing (M.S dissertation, Missouri University of Science and Technology).

Ayers, J.C., and Watson, E.B. (1993). Apatite/fluid partitioning of rare-earth elements and strontium: Experimental results at 1.0 GPa and 1000 C and application to models of fluid-rock interaction. Chemical Geology, 110(1-3), 299-314.

Bédard, J.H. (2009). Parental magmas of Grenville province massif-type anorthosites, and conjectures about why massif anorthosites are restricted to the Proterozoic. Transactions of the Royal Society of Edinburgh 100, 77–103.

Berger, V.I., Singer, D.A., and Orris, G.J. (2009). Carbonatites of the World, Explored Deposits of Nb and REE--database and Grade and Tonnage Models (pp. 1-17). Reston, Virginia: US Geological Survey.

BM Review. (2022). Identifying the pinch points in the LFP supply chain. Battery Materials Review 5(2), 1-4.

Bonsack, J.P. (1970). Titanium Dioxide Pigment. Liquid-Liquid Extraction of Chromium. Industrial & Engineering Chemistry Product Research and Development, 9(3), 398-403.

Chandra, K., Mahanti, A., Kain, V., Kumar, B.S., Kumar, N., and Gautam, V. (2017). Failure cases related to material issues in wet-process phosphoric acid plant. Engineering Failure Analysis, 79, 642-655.

Charlier, B., Namur, O., Bolle, O., Latypov, R., and Duchesne, J.C. (2015). Fe–Ti–V–P ore deposits associated with Proterozoic massif-type anorthosites and related rocks. Earth-Science Reviews, 141, 56-81.

Cruz, F.F., Chaban, N., Machado, P.T., Townend, R., and Machado, J.E. (1976). Aspects of the superficial phosphorus and titanium deposits of the Tapira carbonatite complex, Minas Gerais, Brazil. 25th International Geological Congress, Australia, Abstracts, 1: 209-10.

Darezereshki, E., Khodadadi Darban, A., and Abdollahy, M. (2018). Synthesis of magnetite nanoparticles from iron ore tailings using a novel reduction-precipitation method. Journal of Alloys and Compounds, 749, 336-343.

de Oliveira, S.M.B., and Imbernon, R.A.L. (1998). Weathering alteration and related REE concentration in the Catalão I carbonatite complex, central Brazil. Journal of South American Earth Sciences, 11(4), 379-388.

El Bamiki, R., Raji, O., Ouabid, M., Elghali, A., Khadiri Yazami, O., and Bodinier, J. L. (2021). Phosphate Rocks: A Review of Sedimentary and Igneous Occurrences in Morocco. Minerals, 11(10), 1137.

European Commission. (2020). Communication from the commission to the European Parliament, the Council, the European Economic, and Social Committee, and the Committee of the regions. Critical Raw Materials Resilience: Charting a Path towards greater Security and Sustainability COM/ 2020/4.

Fourie, P.J., and De Jager, D.H. (1986). Phosphate in the Phalaborwa complex. In C.R. Anhaeusser and S. Maske (eds) Mineral deposits of Southern Africa, 2: 2239-53. The Geological Society of South Africa, Johannesburg.

Goldoff, B., Webster, J D., and Harlov, D.E. (2012). Characterization of fluor-chlorapatites by electron probe microanalysis with a focus on time-dependent intensity variation of halogens. American Mineralogist, 97(7), 1103-1115.

Government of Ontario. (2022). Ontario's Critical Minerals Strategy: Unlocking potential to drive economic recovery and prosperity. 53 pages.

Grant, M. (2020). Formation of Magmatic Fe-Ti-VP Deposits Within the Lac St. Jean Area Saguenay, Québec, Canada: Insights from Trace Element Composition of Fe-Oxides and Apatite (M.Sc dissertation, Université d'Ottawa/University of Ottawa).

Hébert, C., Cadieux, A. M., and van Breemen, O. (2005). Temporal evolution and nature of Ti–Fe–P mineralization in the anorthosite–mangerite–charnockite–granite (AMCG) suites of the south-central Grenville Province, Saguenay–Lac St. Jean area, Québec, Canada. Canadian Journal of Earth Sciences 42, 1865–80.

Higgins, M.D., and van Breemen, O. (1992). The age of the Lac-Saint-Jean Anorthosite Complex and associated mafic rocks, Grenville Province, Canada. Canadian Journal of Earth Sciences 29, 1412–1423.

Higgins, M.D., and van Breemen, O. (1996). Three generations of Anorthosite–Mangerite–Charnockite–Granite magmatism, contact metamorphism and tectonism in the Saguenay-Lac-St-Jean region, Grenville Province, Canada. Precambrian Research 79, 347–362.

Higgins, M. D., Ider, M., and van Breemen, O. (2002). U–Pb ages of plutonism, wollastonite formation, and deformation in the central part of the Lac-Saint-Jean anorthosite suite. Canadian Journal of Earth Sciences 39, 1093–105.

Jochum, K.P., Weis, U., Stoll, B., Kuzmin, D., Yang, Q., Raczek, I., Jacob, D.E., Stracke, A., Birbaum, K., Frick, D.A. and Günther, D. (2011). Determination of reference values for NIST SRM 610–617 glasses following ISO guidelines. Geostandards and Geoanalytical Research, 35(4), 397-429.

Jochum, K.P., Willbold, M., Raczek, I., Stoll, B., and Herwig, K. (2005). Chemical Characterisation of the USGS Reference Glasses GSA-1G, GSC-1G, GSD-1G, GSE-1G, BCR-2G, BHVO-2G and BIR-1G Using EPMA, ID-TIMS, ID-ICP-MS and LA-ICP-MS. Geostandards and Geoanalytical Research 29(3), 285-302.

Kim, P. H. (2015). Impurities in Ilmenite: Magnesium (Master's thesis, NTNU).

Ling, J., Karuppiah, C., Krishnan, S.G., Reddy, M.V., Misnon, I.I., Ab Rahim, M.H., Yang, C., and Jose, R. (2021). Phosphate polyanion materials as high-voltage lithium-ion battery cathode: a review. Energy & Fuels, 35(13), 10428-10450.

Mikhailova, J. A., Kalashnikov, A.O., Sokharev, V.A., Pakhomovsky, Y.A., Konopleva, N.G., Yakovenchuk, V. N., Bazai, A.V., Goryainov, P.M., and Ivanyuk, G.Y. (2016). 3D mineralogical mapping of the Kovdor phoscorite–carbonatite complex (Russia). Mineralium Deposita, 51(1), 131-149.

Mineral Commodity Summaries (2022). US Geological Survey: Reston, VA, USA, 2022. 202 pages.

O'Brien, H., Heilmo, E., and Geino, P. (2015). The Archean Silinjärvi Carbonatite Complex. Mineral Deposits of Finland, 327-343.

Owens, C.L., Nash, G.R., Hadler, K., Fitzpatrick, R.S., Anderson, C.G., and Wall, F. (2019). Apatite enrichment by rare earth elements: A review of the effects of surface properties. Advances in colloid and interface science, 265, 14-28.

P& E Mining Consultants Inc. (2022). Technical report and initial mineral resource estimate of the Lac Original phosphate property, northern Quebec. 205 pages.

Prowatke, S., and Klemme, S. (2006). Trace element partitioning between apatite and silicate melts. Geochimica et Cosmochimica Acta, 70(17), 4513-4527.

Padhi, A.K., Nanjundaswamy, K.S., and Goodenough, J.B. (1997). Phospho-olivines as positive-electrode materials for rechargeable lithium batteries. Journal of the electrochemical society, 144(4), 1188-1194.

Paton, C., Hellstrom, J., Paul, B., Woodhead, J., and Hergt, J. (2011). Iolite: Freeware for the visualisation and processing of mass spectrometric data. Journal of Analytical Atomic Spectrometry, 26(12), 2508-2518.

Peng, B., Ma, Z., Zhu, Y., and Tang, L. (2022). Release and recovery of fluorine and iodine in the production and concentration of wet-process phosphoric acid from phosphate rock. Minerals Engineering, 188, 107843.

Piccoli, P.M., and Candela, P.A. (2002). Apatite in igneous systems. Reviews in Mineralogy and Geochemistry, 48(1), 255-292.

Pourmand, A., Dauphas, N., and Ireland, T.J. (2012). A novel extraction chromatography and MC-ICP-MS technique for rapid analysis of REE, Sc and Y: Revising CI-chondrite and Post-Archean Australian Shale (PAAS) abundances. Chemical Geology, 291, 38-54.

Pufahl, P.K., and Groat, L.A. (2017). Sedimentary and igneous phosphate deposits: formation and exploration: an invited paper. Economic Geology, 112(3), 483-516.

Rivers, T., Martignole, J., Gower, C.F., and Davidson, A. (1989). New tectonic divisions of the Grenville Province, southeastern Canadian Shield. Tectonics, 8, 63–84.

Rocha, M.L.B.P., Barros, M.A.d.S.A., de Lima, E.F., and Pierosan, R., (2012). Paleoproterozoic Domo of Lava from Iriri Group- Sonho Meu Farm- Northeast of Mato Grosso, Amazon

Craton: geology, geochemistry, and geochronology. Revista Brasileira de Geociencias 42, 471-488.

Rollinson, H. R. (2014). Using geochemical data: evaluation, presentation, interpretation. Routledge.

Schorr, M., and Valdez, B. (2017). Phosphoric Acid Industry: Problems and Solutions. BoD – Books on Demand.

Schorr, M., Valdez, B., Zlatev, R., and Stoytcheva, M. (2010). Phosphate ore processing for phosphoric acid production: classical and novel technology. Mineral Processing and Extractive Metallurgy, 119(3), 125-129.

Schulz, K.J., DeYoung, J.H.J., Seal II, R.R., and Bradley, D.C. (2017). Critical Mineral Resources of the United States - Economic and Environmental Geology and Prospects for Future: U.S. Geological Survey Professional Paper 1802. U.S. Geological Survey.

SGS (2022a). Report on mineral composition for the Lac Original phosphate property, project no 19397-01 LIMS#5008-AUG22. 16 pages.

SGS (2022b). SGS Minerals Services Preliminary Report on composite samples (n=75) mineral composition for the Lac Original phosphate property, project no 19397-01, Aug 17th, 2022. 3pages.

Spears, B.M., Brownlie, W.J., Cordell, D., Hermann, L., and Mogollón, J.M. (2022). Concerns about global phosphorus demand for lithium-iron-phosphate batteries in the light electric vehicle sector. Communications Materials, 3(1), 1-2.

Stormer, J.C., Pierson, M.L., and Tacker, R.C. (1993). Variation of F and Cl X-ray intensity due to anisotropic diffusion in apatite during electron microprobe analysis. American Mineralogist, 78(5-6), 641-648.

Tornare, E., Pilet, S., and Bussy, F. (2016). Magma differentiation in vertical conduits revealed by the complementary study of plutonic and volcanic rocks from Fuerteventura (Canary Islands). Journal of Petrology, 57(11-12), 2221-2250.

Traversa, G., Gomes, C.B., Brotzu, P., Buraglini, N., Morbidelli, L., Principato, M.S., Ronca, S., and Ruberti, E., (2001). Petrography and mineral chemistry of carbonatites and mica-rich rocks from the Araxa complex (Alto Paranaiba Province, Brazil). An. Acad. Bras. Ci. 72, 71-98.

Verhulst, A., Balaganskaya, E., Kinarsky, Y., and Demaiffe, D., (2000). Petrological and geochemical (trace elements and Sr-Nd isotopes characteristics of the Paleozoic Kovdor ultramafic, alkaline and carbonatite intrusion (Kola Peninsula, NW Russia). Lithos 51, 1-25.

Webster, J.D., and Piccoli, P.M. (2015). Magmatic apatite: A powerful, yet deceptive, mineral. Elements, 11(3), 177-182.

Will, R.K., (2016). The benefits of isolating & utilizing fluorine from phosphate operations. Procedia Engineering, 138, 267-272.

Woodhead, J.D., Hellstrom, J., Hergt, J. M., Greig, A., and Maas, R. (2007). Isotopic and elemental imaging of geological materials by laser ablation inductively coupled plasma-mass spectrometry. Geostandards and Geoanalytical Research, 31(4), 331-343.

Woussen, G., Martignole, J., and Nantel, S. (1988). The Lac-St-Jean anorthosite in the St-Henri-de-Taillon area (Grenville Province): A relict of a layered complex. Canadian Mineralogist, 26, 1013–1025.

Xu, C., Dai, Q., Gaines, L., Hu, M., Tukker, A., and Steubing, B. (2020). Future material demand for automotive lithium-based batteries. Communications Materials, 1(1), 1-10.

Ye, N., Yan, T., Jiang, Z., Wu, W., and Fang, T. (2018). A review: conventional and supercritical hydro/solvothermal synthesis of ultrafine particles as cathode in lithium battery. Ceramics International, 44(5), 4521-4537.

Zieg, M.J., and Wallrich, B.M., (2018). Emplacement and Differentiation of the Black Sturgeon Sill, Nipigon, Ontario: a principal component analysis. Journal of Petrology, 59(12), 2385-2412.